# 13. Refractory Metals and Refractory Metal Alloys

Wolfram Knabl, Gerhard Leichtfried, Roland Stickler

Refractory metals belong to the 5th and 6th group of the periodic system of elements and have a melting point above 2000 °C. Examples are Nb, Ta, Mo and W.

This chapter provides an overview of this class of materials. After a review of different production routes, the typical compositions of commercial refractory metal alloys and their applications are described. Physical and chemical properties are listed and the recrystallization behavior, as well as the mechanical properties including low- and high-cycle fatigue, are depicted. The mechanisms leading to an increased recrystallization temperature by either doping Mo and W with rare earth oxides or by K-doping of W are explained. Furthermore, fracture mechanics and creep properties are described and an extensive compilation of materials data is included.

In addition to a high melting point, the metals Nb, Ta, Mo, and W have a low coefficient of thermal expansion, a low vapor pressure, and an excellent corrosion resistance against acids, liquid metals and ceramic melts. Mo and W have a high thermal and electrical conductivity, a high Young's modulus and mechanical properties, which strongly depend on the content of interstitial impurities such as oxygen, sulfur, phosphorous, nitrogen, carbon and boron. The interrelationships are summarized in this chapter.



Several books and reviews have been published on the technology and properties of refractory metals and their alloys [13.1–10]. According to the most common definition, refractory metals comprise elements of the group 5 and 6 with a melting point higher than 2000 °C; these are Nb, Ta, Mo, and W. In some publications the group 7 metal Re is also included, as it does not fit in any other classification. Less common definitions describe a refractory metal as a metal with a melting point equal to or greater than that of Cr, thus additionally including V, Tc, the reactive metal Hf, and the noble metals Ru, Os, and Ir. This chapter will give data on Mo, W, Ta, Nb, and their alloys.

Powder metallurgy (P/M) is the only production route for commercial W and W alloys and for more than 97% of Mo and Mo alloys, the remainder is processed by electron-beam melting (EB) and vacuum-arc casting (VAC) [13.11]. The finer grain structure of P/M-material is advantageous for both the further processing and the mechanical properties of the finished product. For some alloys such as those doped with K-silicate, $La_2O_3$, $Ce_2O_3$ and $Y_2O_3$, P/M is the only possible production technique.

The mechanical properties and the homogenous microstructure required are again the reasons to apply P/M in producing Ta wire as widely employed in the manufacture of capacitors. The larger fraction of the Ta sheet production is based on the use of EB melted sheet bars, as this is more economical. The techniques of VAC and EB dominate in the production of Nb and Nb alloys.


W. Martienssen, H. Warlimont (Eds.), *Springer Handbook of Materials Data*, https://doi.org/10.1007/978-3-319-69743-7_13

The industrial P/M production routes of Mo, W, Ta, and their alloys are given in Fig. 13.1. Net shape techniques such as powder injection molding, spraying on a lost core (vacuum-plasma-spraying, chemical vapor deposition) and selective laser melting are limited to some specific applications in the field of electronic and medical devices as well as aerospace products.

Less than 10% of the production quantity is delivered in the as-sintered state. The most common fully-dense-processing techniques are deformation by rolling, forging, swaging, and drawing.

In the very beginning of the industrial use of refractory metals in the 1920s, they were applied mainly in the technically pure state. In the 1960s and 1970s extensive developments were driven by US aerospace programs leading to a wide variety of alloys now commercially available. Since then key applications mainly in the field of electronics and lighting have been the key-drivers for further development.

The compositions of solid solution, precipitation- and dispersion-strengthened alloys are given in Table 13.1. W heavy metals and refractory-metal-based composite materials are not included here. Carbide precipitation hardening of Mo (in the Mo-Ti-Zr-C alloy TZM and in the Mo-Hf-C alloy MHC) is effective up to 1400 °C. The addition of the deformable oxides $La_2O_3$ (in the lanthania doped Mo – ML) and $xK_2O \cdot ySiO_2$ (in K-Si-Mo), respectively, results in oxide refinement by deformation and in the possibility of tailoring the mechanical properties. This is the main alloying mechanism for Mo applied in lamps [13.13–16]. Solid solution alloying (e.g., Mo-W, Mo-Nb, Mo-Ta) allows to adapt the physical and chemical properties to a wide variety of applications in the field of electronics.

The W alloy which is commercially most important is Al-K-silicate doped W (AKS-W). It is a dispersion-strengthened, micro-alloyed metal with a directionally recrystallized microstructure. Spherical bubbles stabilized at operating temperature by the vapour pressure of the inclosed K-gas are interacting with dislocations, sub-boundaries and high-angle boundaries [13.17, 18]. The high stability of these bubbles can be explained by the low solubility of K in W, even at operating temperatures up to 3200 °C.

A continual task is to reduce the low-temperature brittleness of Mo and W, which is essentially due to a rigid covalent component of the interatomic bonds along the edges of the bcc unit cell. This causes a low solubility for interstitial elements which occupy the octahedral sites of the lattice and give rise to its tetragonal distortion and a strong interaction of dislocations with the elastic strain field surrounding the interstitial solutes, thus impeding the dislocation movement [13.19]. One possibility to increase the low-temperature ductility is alloying with Re which lowers the brittle-to-ductile-transition temperature of both W and Mo [13.20–22]. But the insufficient supply and the high price of Re limit the application of these alloys.

The addition of oxides such as $La_2O_3$, $Ce_2O_3$, $ThO_2$, BaO, SrO, $Y_2O_3$, and $Sc_2O_3$ lowers the electron work function of W, which is important for its application in electrodes. The production quantities of W-$La_2O_3$, W-$La_2O_3$-$ZrO_2$ and W-$Ce_2O_3$ as electron emitting materials are increasing at the expense of the slightly radioactive W-$ThO_2$ material.

The production of capacitors, the dominating application of Ta, requires material in its purest state. Solid-

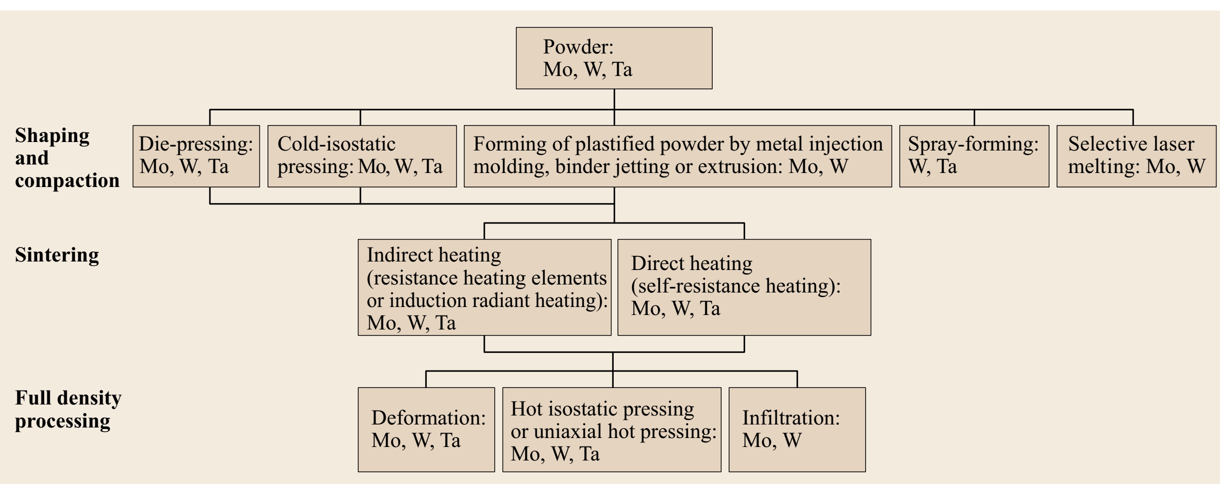


**Fig. 13.1** Large-scale P/M production routes for Mo, W and Ta (after [13.12])

**Table 13.1** Typical compositions of commercial refractory metal alloys (in weight percent, analyses of base-metal correspond to metallic purity) (after [13.12])

| Alloy designation | Mo | W | Ta | Nb | Re | C | O | Si | K | Y | La | Ce | Th | Ti | Zr | Hf |
|---|---|---|---|---|---|---|---|---|---|---|---|---|---|---|---|---|
| **Molybdenum alloys** | | | | | | | | | | | | | | | | |
| Pure Mo | 99.97 | | | | | | | | | | | | | | | |
| TZM | Bal | | | | | 0.025 | | | | | | | | 0.5 | 0.08 | |
| MHC | Bal | | | | | 0.08 | | | | | | | | | | 1.2 |
| Mo-$La_2O_3$ (ML) | Bal | | | | | | 0.004–0.15 | | | | 0.026–0.85 | | | | | |
| Mo-$Y_2O_3$ (MY) | Bal | | | | | | 0.10–0.12 | | | 0.37–0.43 | | 0–0.06 | | | | |
| Mo-$ZrO_2$ (MZ) | Bal | | | | | | 0.43 | | | | | | | | 1.24 | |
| K-Si-Mo | Bal | | | | | | 0.01–0.07 | 0.013–0.070 | 0.005–0.03 | | | | | | | |
| Mo 3–9.7 Nb | Bal | | | 3.0–9.7 | | | | | | | | | | | | |
| Mo10.7Ta | Bal | | 10.7 | | | | | | | | | | | | | |
| Mo 41–47.5 Re | Bal | | | | 41.0–47.5 | | | | | | | | | | | |
| Mo 10–50 W | Bal | 10–50 | | | | | | | | | | | | | | |
| **Tungsten alloys** | | | | | | | | | | | | | | | | |
| Pure W | | 99.99 | | | | | | | | | | | | | | |
| UHP-W | | 99.9995 | | | | | | | | | | | | | | |
| AKS-W | | Bal | | | | | | | 0.004–0.01 | | | | | | | |
| W-$La_2O_3$ (WL) | | Bal | | | | | 0.15–0.30 | | | | 0.85–1.7 | | | | | |
| W-$Ce_2O_3$ (WC) | | Bal | | | | | 0.29 | | | | | 1.71 | | | | |
| W-$La_2O_3$-$ZrO_2$ (WLZ) | | Bal | | | | | 0.39 | | | | 2.13 | | | | 0.05 | |
| W-$ThO_2$ (WT) | | Bal | | | | | 0.24 | | | | | | 1.76 | | | |
| AKS-W-$ThO_2$ | | Bal | | | | | 0.12–0.24 | | 0.001–0.005 | | | | 0.88–1.76 | | | |
| W 3–26 Re | | Bal | | | 3.0–26.0 | | | | | | | | | | | |
| AKS-W3Re | | Bal | | | 3.0 | | | | 0.004 | | | | | | | |
| **Tantalum alloys** | | | | | | | | | | | | | | | | |
| Pure Ta | | | 99.95 | | | | | | | | | | | | | |
| Ta 2.5–10 W | | 2.5–10.0 | Bal | | | | | | | | | | | | | |
| **Niobium alloys** | | | | | | | | | | | | | | | | |
| Pure Nb | | | | 99.9 | | | | | | | | | | | | |
| Nb1Zr | | | | Bal | | | | | | | | | | | 1.0 | |
| C-103 | | | | Bal | | | | | | | | | | 1.0 | | 10.0 |
| FS-85 | | 10.0 | 28.0 | Bal | | | | | | | | | | | 1.0 | |
| WC-3009 | | 9.0 | | Bal | | | | | | | | | | | | 30.0 |
| Nb46.5Ti | | | | Bal | | | | | | | | | | 46.5 | | |

solution-strengthened Ta2.5W is used for components in chemical apparatus. Superconducting Nb46.5Ti accounts for more than half of all Nb alloys produced. Zr and Hf are the main additions for Nb-based alloys used by the lighting and aerospace industry.

The producers of electrical and electronic devices, including the lighting industry, are the largest consumers of refractory metal products. The amount of Mo, Mo-W, Mo-Nb, and Mo-Ta sputtering targets applied in the production of wiring for displays, e.g., thin-film transistor (TFT) liquid crystal displays (LCDs), has risen significantly owing to the unique combination of low electrical resistivity, hillock suppression, barrier characteristic and the ability of forming an ohmic contact with many functional materials, such as $n^+$-Si and indium-tin oxide (ITO). Rapid growth in multimedia and wireless communication networks systems has boosted the need for W-Cu and Mo-Cu heat sink materials. These materials possess a high thermal conductivity combined with a low thermal expansion, close to those of Si, GaAs and GaN semiconductors or certain packaging materials. Further important products are semiconductor base-plates for power rectifiers, components for ion implantation equipment and electrical contacts, e.g., W-Cu for $SF_6$ circuit breakers. The electronic industry is also by far the largest market for Ta based products, employing the metal mainly in the manufacture of capacitors and integrated circuits with Cu interconnects. Significant quantities of W and Mo are still used in various products for lamps, such as electrodes, filaments, support wires or dipped beam shields. Besides that, refractory metals and their alloys are used in a wide variety of applications and products such as advanced material processing, medical equipment; automotive, aerospace, and defense industry; chemical and pharmaceutical industry; or premium and sporting goods.

Examples of products used in advanced material processing are Mo and W crucibles for the production of sapphire single crystals, Mo glass melting electrodes, TZM and MHC isothermal forging tools, weighing several tons per part, TZM piercing plugs for the production of stainless steel tubes, Mo and Ta crucibles for synthesizing artificial diamond, or TIG welding electrodes.

In order to improve the tribological properties of transmission and engine components for automobiles they are coated with Mo.

Products in the field of aerospace and defense industry are rocket nozzles, kinetic energy (KE) penetrators, shaped charge liners (SCLs) and explosively formed penetrators (EFPs).

The rotating x-ray anode, a composite product made of W5Re or W10Re, TZM or MHC and optionally graphite, is the essential item of medical x-ray tubes for computed tomography (CT) scanning and angiography systems.

## 13.1 Physical Properties

The atomic and structural properties of the pure refractory metals are listed in Chap. 4, Tables 4.75–4.80 and Tables 4.88–4.94. Special features of refractory metals are their low vapor pressure, low coefficient of thermal expansion, and the high thermal and electrical conductivity of Mo and W. This combination of physical properties has opened up a wide range of new applications during the last decade, especially in the field of electronics.

The coefficient of linear thermal expansion, the thermal conductivity, the specific heat, and the electrical resistivity as function of temperature are shown in Figs. 13.2–13.5. The vapor pressure and rate of evaporation are shown in Fig. 13.6. In the case of precipitation- and dispersion-strengthened Mo alloys, such as TZM, MHC, ML, MY, and K-Si-Mo, as well as the W based alloys AKS-W, WL, WC, and WT, the physical properties do not differ significantly from those of the pure metals. Values for the Young's modulus and its temperature dependence are plotted in Fig. 13.7. The Young's moduli of the group 5 metals are considerably lower than those of the group 6 metals due to the differences in electronic structure.

The strong influence of the surface conditions on the emissivity and lack of information in the literature con-

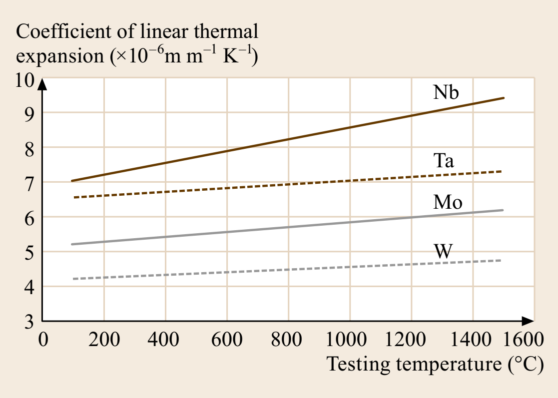


**Fig. 13.2** Coefficient of linear thermal expansion versus temperature of Mo (after [13.23]), W (after [13.23]), Nb (after [13.24]), and Ta (after [13.25])

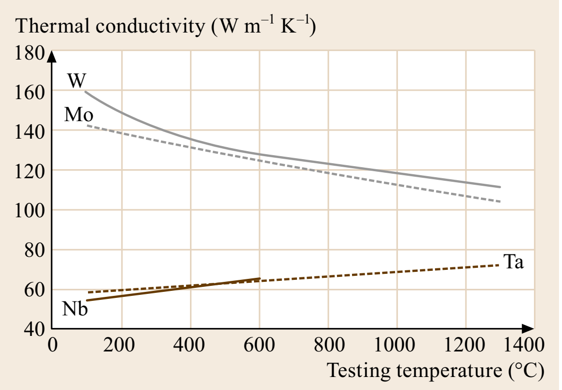


**Fig. 13.3** Thermal conductivity versus testing temperature of Mo (after [13.23]), W (after [13.26]), Nb (after [13.24]), and Ta (after [13.24])

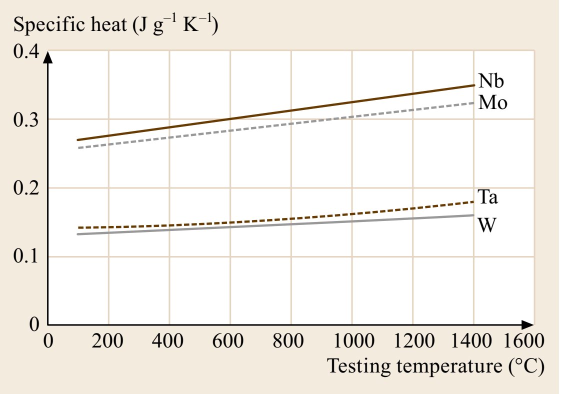


**Fig. 13.4** Specific heat versus testing temperature of Mo, W, Nb, and Ta (after [13.23])

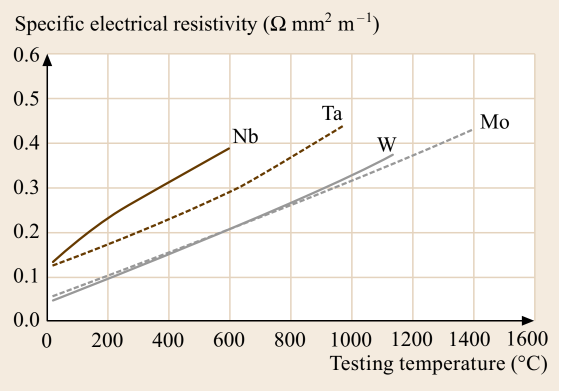


**Fig. 13.5** Specific electrical resistivity versus testing temperature of Mo (after [13.23]), W (after [13.23]), Nb (after [13.24]), and Ta (after [13.24])

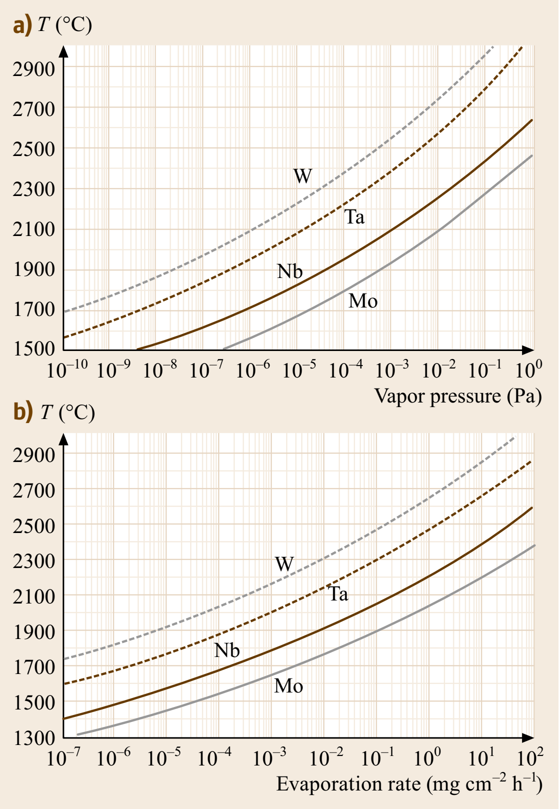


**Fig. 13.6a,b** Vapor pressure **(a)** and evaporation rate **(b)** versus temperature of Mo, W, Nb, and Ta (after [13.26])

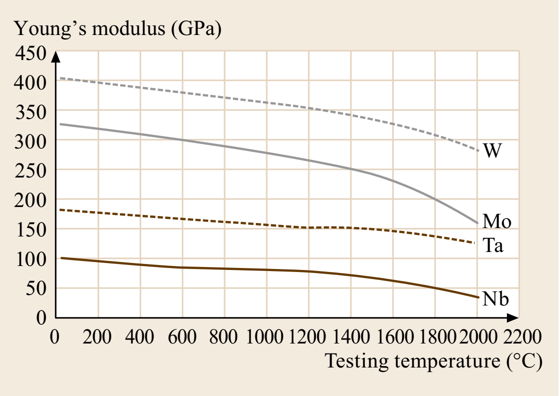


**Fig. 13.7** Young's moduli versus testing temperature of Mo, W, Nb, and Ta (after [13.25])

cerning pre-treatment make it difficult to interpret emissivity data. An overview of emissivity measurements for W, Nb, and Ta at 684.5 nm from 1500 °C up to the liquid phase using laser polarimetry is given in [13.27].

## 13.2 Chemical Properties

Refractory metals are highly resistant to many chemical agents. Ta is outstanding in its performance as it is inert to all concentrations of hydrochloric and nitric acid, 98% sulfuric acid, 85% phosphoric acid, and aqua regia below 150 °C. Ta is attacked by hydrofluoric acid and strong alkalis, however. The excellent corrosion resistance of Ta is attributed to dense natural oxide layers which prevent the chemical attack of the metal. Nb is less resistant than Ta and embrittles more easily. Nevertheless the more economical Nb has replaced Ta in some applications. Mo and W are highly resistant to many molten glasses and metals as long as free oxygen is absent.

The interaction with H, N, and O is widely different for Mo and W on the one hand, and Nb and Ta on the other. Mo and W have almost no solubility, whereas Nb and Ta can dissolve a considerable amount of these elements. H can be removed from Nb at 300–1600 °C and from Ta at 800–1800 °C without metal loss by degassing in high vacuum. For the removal of N in high vacuum, temperatures higher than 1600 °C are recommended. The evaporation of volatile oxides at temperatures above 1600 °C in high vacuum leads to a reduction of the oxygen content in Nb and Ta. However during such heat treatments, metal is evaporated simultaneously.

An overview on the resistance of pure Mo, W, Nb, and Ta against different media is given in Tables 13.2–13.4. In accordance with the definition given in [13.28], a material is considered *stable* against a corrosive medium if the metal loss is $< 0.1\,\mathrm{mm\,yr^{-1}}$. If the loss of material is between 0.1 and $1.0\,\mathrm{mm\,yr^{-1}}$, the

**Table 13.2** Metal loss of Mo, W, Nb and Ta in millimeter per year ($\mathrm{mm\,yr^{-1}}$) in acids, alkalis and salt solutions

| Corroding agent (aqueous solution) | Temperature | Metal loss ($\mathrm{mm\,yr^{-1}}$) Mo | W | Nb | Ta |
|---|---|---|---|---|---|
| 10% HCl | 20 °C | < 0.003 | 0.002 | 0 | < 0.001 |
| 10% $H_2SO_4$ | 20 °C | < 0.005 | < 0.1 | < 0.1 | < 0.1 |
| 10% $HNO_3$ | 20 °C | 18.6 | < 0.25 | < 0.013 | < 0.013 |
| 3% HF | 20 °C | < 0.001 | < 0.1 | > 3.0 | > 3.0 |
| 10% $CH_3COOH$ | 20 °C | 0.07 | < 0.05 | < 0.1 | < 0.013 |
| 10% KOH | 20 °C | < 0.1 | < 0.1 | < 0.2 | < 0.1 |
| 3% NaCl | 20 °C | < 0.1 | < 0.1 | < 0.1 | < 0.1 |
| 10% HCl | 100 °C | < 0.025 | 0.005 | 0.005 (embrittlement) | < 0.025 |
| 10% $H_2SO_4$ | 100 °C | 0.17 | < 0.25 | < 0.001 | 0 |
| 10% $HNO_3$ | 100 °C | 150 | < 0.25 | < 0.076 | < 0.025 |
| 3% HF | 100 °C | 0.18 | 0.15 | > 3.0 | > 3.0 |
| 10% $CH_3COOH$ | 100 °C | 0.033 | < 0.05 | < 0.1 | < 0.013 |
| 10% KOH | 100 °C | 0.054 | 0.01 | 1.2 (embrittlement) | < 0.003 (embrittlement) |
| 3% NaCl | 100 °C | < 0.1 | < 0.1 | < 0.1 | < 0.1 |

**Table 13.3** Maximum temperatures for the resistance of Mo, W, Nb, and Ta against metal melts (up to the stated temperatures the solubility of the refractory metal in the metal melts and vice versa is negligible)

| Metal melt | Maximum resistance temperature (°C) Mo | W | Nb | Ta |
|---|---|---|---|---|
| Al | Not resistant | 680 | Not resistant | Not resistant |
| Pb | 1100 | 1100 | 850 | 1000 |
| Fe | Not resistant | Not resistant | Not resistant | Not resistant |
| Ga | 300 | 800 | 400 | 450 |
| K | 1200 | 900 | 1000 | 1000 |
| Cu | 1300 | Resistant | Resistant | Resistant |
| Mg | 1000 | 600 | 950 | 1150 |
| Na | 1030 | 900 | 1000 | 1000 |
| Hg | 600 | 600 | 600 | 600 |
| Zn | 500 | 750 | Not resistant | 500 |
| Sn | 550 | 980 | Not resistant | 260 |
| Ag | Resistant | Resistant | Resistant | 1200 |

**Table 13.4** Maximum temperatures for the resistance of Mo, W, Nb, and Ta against gaseous media at atmospheric pressure

| Gaseous media | Maximum resistance temperature | | | |
|---|---|---|---|---|
| | Mo | W | Nb | Ta |
| Air and oxygen | Sect. 13.2 | | | |
| Hydrogen | Resistant | Resistant | 250 °C ($T > 250$ °C embrittlement owing to dissolved hydrogen) | 300 °C ($T > 300$ °C embrittlement owing to dissolved hydrogen) |
| Nitrogen | Resistant | Resistant | 300 °C ($T > 300$ °C embrittlement owing to dissolved nitrogen) | 400 °C ($T > 400$ °C embrittlement owing to dissolved nitrogen) |
| Ammonia | Resistant (except 1000–1100 °C: nitration) | Resistant (except 700–1150 °C: nitration) | 300 °C ($T > 300$ °C embrittlement owing to dissolved nitrogen) | 700 °C ($T > 700$ °C embrittlement owing to dissolved nitrogen) |
| Water vapor | 700 °C | 700 °C | 200 °C | 200 °C |
| Carbon monoxide | 800 °C ($T > 800$ °C carburization) | 1000 °C ($T > 800$ °C carburization) | 800 °C | 1100 °C |
| Carbon dioxide | 1200 °C ($T > 1200$ °C oxidation) | 1200 °C ($T > 1200$ °C oxidation) | 400 °C | 500 °C |

material is *considerably stable*; and it is *fairly unstable* if the loss of material is between 1.0 and 3.0 mm. The material is *unsuitable* in an environment if the metal loss is $> 3.0\,\mathrm{mm\,yr^{-1}}$.

The special feature of Mo and W to form thermodynamic stable compounds, e.g., with Si, O, S and Se, at temperatures below 500 °C, which are electrically conducting or semiconducting, makes them an attractive metal for some thin film applications (e.g., microelectronics, TFT LCDs and solar cells). Essential is the formation of an ideal ohmic contact to Si, to metal oxides such as indium-tin-oxide (ITO) or chalcopyrite compounds such as copper-indium-gallium-diselenide (CIGS) [13.29–31].

### 13.2.1 Oxidation Behavior

Refractory metals require protection from oxidizing environment as they do not form protective oxide layers. Oxidation of Mo and W leads to a loss of material by the formation of volatile oxides above 600 °C for Mo and 750 °C for W, respectively, but without any significant impact on the mechanical properties. The low temperature oxidation of Mo and W often causes problems in practical use as thin corrosion films are formed during storage in moist air. The surface topography of Mo has a strong impact on the reaction rate. The corrosion film contains oxygen but also chemically-bonded nitrogen, which is incorporated in the film during film growth. $C_xH_y$ residues are the nuclei for the oxidative attack in the early stage of film growth [13.32].

Especially sputtered Mo films used for TFT LCDs and touch sensors need improved corrosion resistance in humid ambient atmosphere. For these applications Mo alloys such as Mo-Ta and Mo-Nb have been developed [13.34]. There is extensive evidence that between 300 and 500 °C, oxide-dispersion-strengthened (ODS) refractory metal alloys (e.g., Mo-$La_2O_3$ and Mo-$Y_2O_3$ grades) possess markedly reduced oxidation rates compared to the pure metals [13.33]. In-situ oxidation and evaluation of the binding state reveal that $MoO_2$ dominates over $MoO_3$ both for Mo and Mo-0.47 wt% $Y_2O_3$-0.08 wt% $Ce_2O_3$ (Fig. 13.8). These results are confirmed when comparing the thickness of the oxide layer formed at 500 °C in air (Fig. 13.9). The enhanced oxidation resistance of doped samples cannot be attributed to a chemical but rather to a morphological-mechanical effect. Investigations of the surface of pure Mo samples subjected to long-term oxidation reveal a network of cracks in the $MoO_2$ layer which drastically diminishes the passivating effect of this layer by facilitating a further attack by O. Such cracks cannot be found on the surface of oxidized Mo-$La_2O_3$ and Mo-$Y_2O_3$ samples [13.33].

Above 600 °C for Mo and approximately 750 °C for W, sublimation of the oxides $MoO_3$ and $WO_3$ is the rate-controlling process and the oxidation follows a linear time dependence. Above 2000 °C for Mo and 2400 °C for W, the metal loss increases because of the increasing vapor pressure of the pure metals. The time dependence of metal loss for Mo and W at $T \geq 1200$ °C is shown in Fig. 13.10 [13.35].

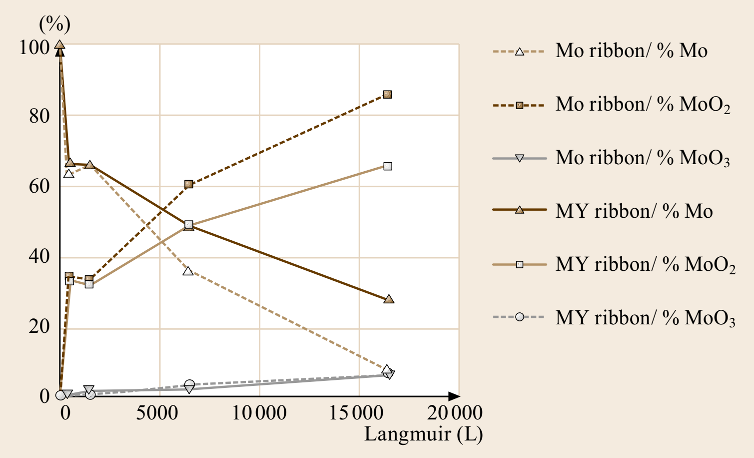


**Fig. 13.8** ESCA measurements and evaluation of $Mo/MoO_2/MoO_3$ fraction versus in-situ oxidation conditions in Langmuir ($1\,L = 10^{-6}$ Torr s). Mo: 4N5 Mo ribbon, electro-polished surface; MY: Mo-0.47 wt% $Y_2O_3$-0.08 wt% $Ce_2O_3$ ribbon, electro-polished surface, test conditions: 500 °C/air (after [13.33])

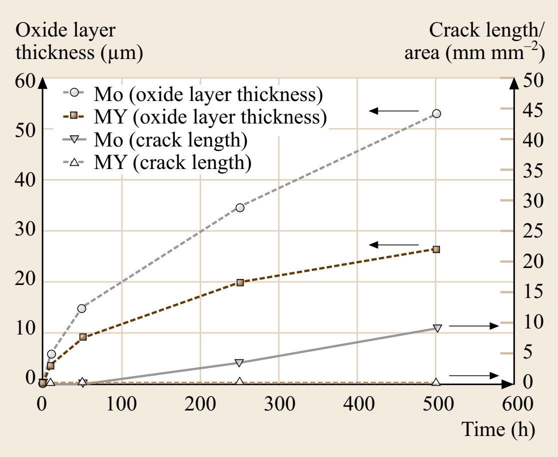


**Fig. 13.9** Thickness of oxide layer and crack length per area versus testing time. Mo: 4N5 Mo ribbon, electropolished surface; MY: Mo-0.47 wt% $Y_2O_3$-0.08 wt% $Ce_2O_3$ ribbon, electropolished surface, test conditions: 500 °C/air (after [13.33]) ◀

The oxidation rates of Nb and Ta strongly depend on temperature, pressure, and time. Different mechanisms causing different oxidation rates can be observed and metastable sub-oxides are formed during use in O-containing atmospheres [13.28, 35]. O is dissolved in the metal matrix which leads to significant changes of the mechanical properties. A poorly adherent, porous pentoxide is formed on the metal surface which does not protect the metal from further attack. O which has penetrated the porous oxide layer diffuses along the

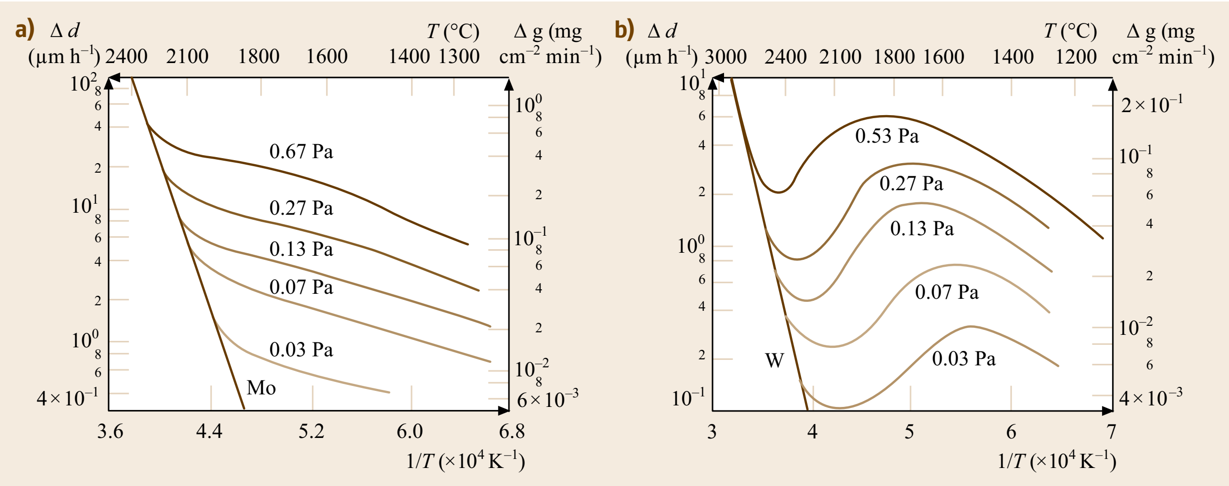


**Fig. 13.10a,b** Metal loss in air for Mo **(a)** and W **(b)** at $T \geq 1200$ °C (after [13.35])

grain boundaries of the metal, leading to drastic embrittlement.

The metal loss at 1100 °C due to oxidation in air is shown for Mo, W, Nb, and Ta in Fig. 13.11 [13.36]. The embrittled zone caused by O diffusion into the substrate is not considered in this diagram.

Only a few coating systems have been found to prevent the refractory metals from oxidation. In the case of Mo, Pt-cladded components with a diffusion barrier interlayer on the basis of alumina, which prevents the formation of brittle intermetallic Mo-Pt phases, are used; e.g., for stirrers used to homogenize special glasses. Mo components for glass tanks and glass melting electrodes are protected from oxidation by coatings based on silicides, such as Si-B [13.37]. Si-B and other silicide based coatings, such as Si-Cr-Fe or Si-Cr-Ti, are also used to protect Mo and Nb based alloys from oxidation in aerospace applications [13.36, 38–40].

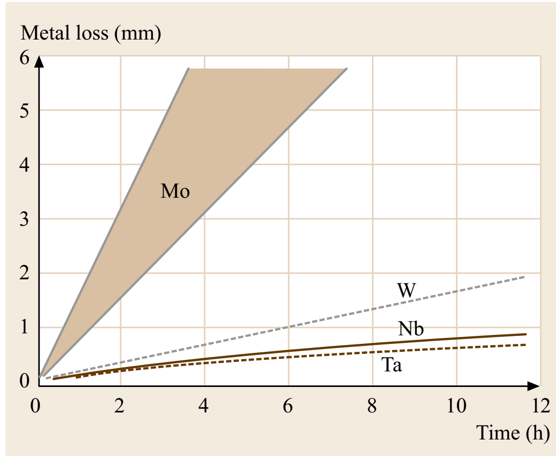


**Fig. 13.11** Oxidation behavior of Mo, W, Nb, and Ta at 1100 °C (after [13.36])

## 13.3 Recrystallization Behavior

The mechanisms and kinetics of recovery and recrystallization processes of the high stacking fault metals Mo and W significantly affect the processing and application of refractory metals. The homologous temperatures ($T/T_M$ in K) for obtaining a 50% recrystallized microstructure during annealing for one hour, range from 0.39 for Mo, 0.41 for W, 0.42 for Nb, to 0.43 for P/M Ta. The fraction of recrystallized structure as a function of the annealing temperature of Mo, W, P/M Ta, TZM, and Mo-0.7 wt% $La_2O_3$ sheets of 1 mm thickness is shown in Fig. 13.12. Experimental data on the evolution of grain size with the annealing temperature for technically pure Mo and Ta sheets of 1 mm thickness are shown in Fig. 13.13 [13.23, 41]. The dependence of grain size on annealing temperature for technically pure Mo deformed by 5% up to 68% has been studied in [13.42]. The results of SEM and TEM investigations on the recovery and recrystallization behavior have been published in [13.43]. A detailed investigation of the influence of the heating rate on the recrystallization behavior of Mo deformed in compression revealed two regimes: at slow heating rates recrystallization is controlled by prerecovery processes, which reduce the driving force for recrystallization, leading to a so-called continuous recrystallization. At fast heating rates such a prerecovery is negligible, and enough stored energy is available for a rapid discontinuous recrystallization [13.44]. Recrystallization diagrams for Mo and W deformed in tension have been published in [13.45] and for P/M Mo deformed in compression in [13.42]. A recrystallization diagram for P/M Ta has been published in [13.46].

Compared to pure Mo, the recrystallization temperature of the carbide-precipitation-hardened alloy TZM is increased by 450 °C and that of Mo-0.7 wt% $La_2O_3$ by 550 °C. The data listed in Table 13.5 show that all those alloys containing particles, which deform to-

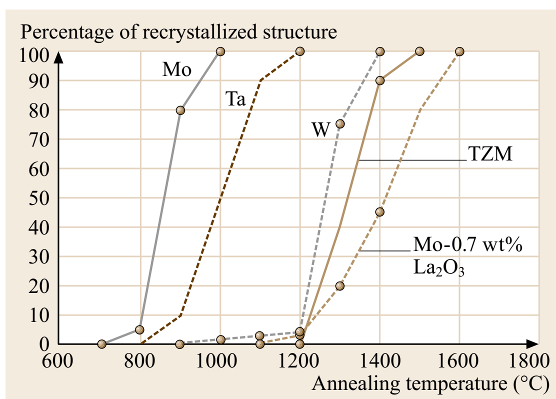


**Fig. 13.12** Fraction of recrystallized structure versus annealing temperature (annealing time $t_a = 1$ h) for Mo, P/M Ta, W, TZM, and Mo-0.7 wt% $La_2O_3$ sheets with a thickness of 1 mm, degree of deformation, $\varphi = (th_p - th_s)/th_p \cdot 100$ [%], where $th_p$ = thickness of sintered plate, and $th_s$ = thickness of rolled sheet. Mo: $\varphi = 94\%$, P/M Ta: $\varphi = 98\%$, W: $\varphi = 94\%$, TZM: $\varphi = 98\%$, Mo-0.7 wt% $La_2O_3$: $\varphi = 99\%$ (after [13.23])

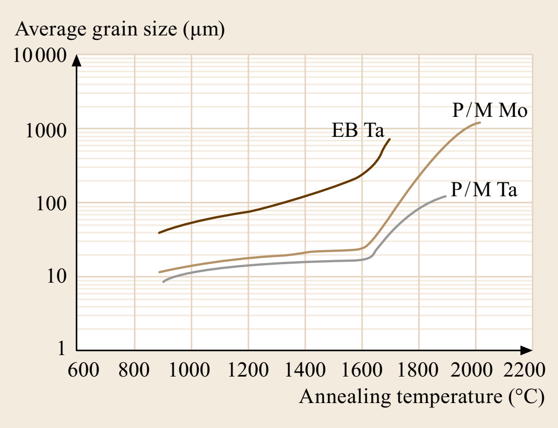


**Fig. 13.13** Grain size versus annealing temperature (annealing time $t_a = 1$ h) for Mo, P/M Ta, and EB Ta sheets with a thickness of 1 mm. Mo: $\varphi = 94\%$, P/M Ta: $\varphi = 98\%$, EB Ta: $\varphi = 98\%$ (after [13.23, 41])

gether with the matrix metal (ML, K-Si-Mo, WL10, WL15, WT20, and AKS-W-$ThO_2$), reveal a significantly increased recrystallization temperature in the highly deformed state. Increasing the degree of deformation from $\varphi = 90\%$ to $\varphi = 99.99\%$ leads to a further increase of the recrystallization temperature (100% recrystallized structure, 1 h annealing time) ranging from 600 °C for K-Si-Mo, 700 °C for ML, 950 °C for WT20, 1000 °C for WL10, to 1050 °C for WL15 and WC20. This can be explained by particle refinement. During the deformation process the particles are elongated. During annealing they break up and rows of smaller particles are formed. With the increase in number of particles, the subgrain boundaries are pinned more effectively, resulting in an increase of the recrystallization temperature [13.13].

Experiments with various oxide-dispersion-strengthened (ODS) Mo materials with 2 vol.% of oxide, mean oxide particle sizes in the as-sintered state of around 0.8 µm, and a degree of deformation $\varphi = \ln(A_0/A) = 8.5$ ($A_0$: cross section as-sintered, $A$: cross section as deformed), revealed differences in the recrystallization temperature of up to 750 °C depending on the type of oxide used. It could be shown that this effect is caused by particle refinement during deformation and subsequent heat treatment. Particles which increase the recrystallization temperature very effectively, as is the case with $La_2O_3$, show a high particle deformability [13.47].

Whether oxide particles deform in a pseudo-plastic manner or not depends on a multitude of parameters, such as the yield stress of the particles, the yield stress of the matrix, the particle/matrix bonding strength, the crystallite size, the defect density, or the state of stresses. Most of these parameters are unknown or difficult to determine. Good correlation could be found between the particle deformability, with its effect on the increase of the recrystallization temperature, and the fraction of ionic bonding character of the oxide, according to the definition of Pauling [13.47]. Figure 13.14 shows that compounds with a high fraction of ionic bonding character, such as $La_2O_3$ or SrO, raise the recrystallization temperature very effectively. Slight particle multiplication could

**Table 13.5** Typical recrystallization temperature and ultimate tensile strength of commercial Mo and W based rod and wire materials with a defined degree of total deformation $\varphi$ (after [13.12])

| Alloy designation | Composition (wt%) | Temperature for 100% recrystallized structure ($t = 1$ h) (°C) | Typical ultimate tensile strength at 1000 °C (MPa) |
|---|---|---|---|
| Pure Mo | | 1100 ($\varphi = 90\%$) | 250 ($\varphi = 90\%$) |
| TZM | Mo, 0.5% Ti, 0.08% Zr, 0.025% C | 1400 ($\varphi = 90\%$) | 600 ($\varphi = 90\%$) |
| MHC | Mo, 1.2% Hf, 0.08% C | 1550 ($\varphi = 90\%$) | 800 ($\varphi = 90\%$) |
| ML | Mo, 0.3% $La_2O_3$ | 1300 ($\varphi = 90\%$), 2000 ($\varphi = 99.99\%$) | 300 ($\varphi = 90\%$) |
| MY | Mo, 0.47% $Y_2O_3$, 0.07% $Ce_2O_3$ | 1100 ($\varphi = 90\%$), 1350 ($\varphi = 99.99\%$) | 300 ($\varphi = 90\%$) |
| K-Si-Mo | Mo, 0.05% Si, 0.025% K | 1200 ($\varphi = 90\%$), 1800 ($\varphi = 99.99\%$) | 300 ($\varphi = 90\%$) |
| Mo50Re | Mo, 47.5% Re | 1300 ($\varphi = 90\%$) | 600 ($\varphi = 90\%$) |
| Mo30W | Mo, 30% W | 1200 ($\varphi = 90\%$) | 350 ($\varphi = 90\%$) |
| Pure W | | 1350 ($\varphi = 90\%$) | 350 ($\varphi = 90\%$) |
| AKS-W | W, 0.005% K | 2000 ($\varphi = 99.9\%$) | 800 ($\varphi = 99.9\%$) |
| WL10 | W, 1.0% $La_2O_3$ | 1500 ($\varphi = 90\%$), 2500 ($\varphi = 99.99\%$) | 400 ($\varphi = 90\%$) |
| WL15 | W, 1.5% $La_2O_3$ | 1550 ($\varphi = 90\%$), 2600 ($\varphi = 99.99\%$) | 420 ($\varphi = 90\%$) |
| WC20 | W, 1.9% $Ce_2O_3$ | 1550 ($\varphi = 90\%$), 2600 ($\varphi = 99.99\%$) | 420 ($\varphi = 90\%$) |
| WT20 | W, 2% $ThO_2$ | 1450 ($\varphi = 90\%$), 2400 ($\varphi = 99.99\%$) | 400 ($\varphi = 90\%$) |
| AKS-W-$ThO_2$ | W, 1% $ThO_2$, 0.004% K | 2400 ($\varphi = 99.9\%$) | 1000 ($\varphi = 99.9\%$) |
| W5Re | W, 5 Re | 1700 ($\varphi = 90\%$) | 500 ($\varphi = 90\%$) |
| W26Re | W, 26 Re | 1750 ($\varphi = 90\%$) | 900 ($\varphi = 90\%$) |

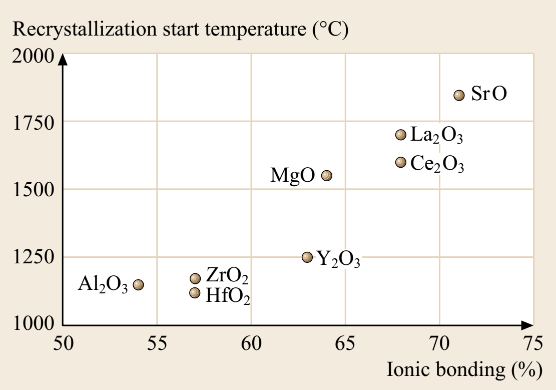


**Fig. 13.14** Recrystallization start temperature of various ODS Mo materials versus fraction of ionic bonding (according to Pauling) of the respective oxides. Oxide content = 2 vol.%, wire diameter = 0.6 mm (after [13.47])

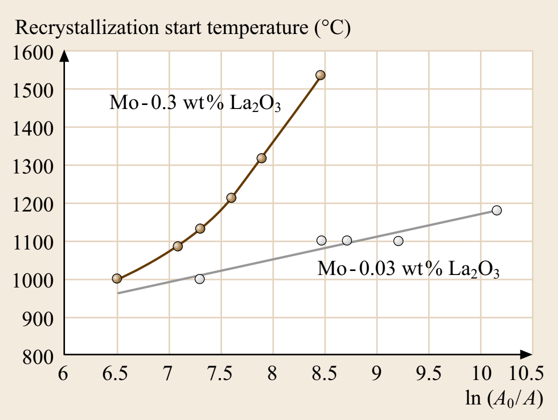


**Fig. 13.15** Recrystallization start temperature of Mo-0.03 wt% $La_2O_3$ and Mo-0.3 wt% $La_2O_3$ wires versus degree of deformation $\ln(A_0/A)$ (after [13.33])

also be found for $Al_2O_3$, $ZrO_2$, and $HfO_2$ compounds with a marked covalent bonding character, because of breakage of the particles during the deformation process.

The recrystallization temperature can be tailored by varying both the type and the content of the oxide, the latter is shown in Fig. 13.15 for Mo-0.03 wt% $La_2O_3$ and Mo-0.3 wt% $La_2O_3$. AKS-W shows a similar effect where the K containing bubbles are effective pinning centers for dislocations and (sub)grain boundaries. The recovery and recrystallization mechanisms of AKS-W as a function of the annealing temperature are summarized in Table 13.6.

The recrystallization temperature of AKS-W is determined by the relation of the driving to dragging forces. The driving forces are determined by the thermomechanical treatment (TMT), the dragging forces depend on the number, size, and distribution of the K bubbles. With increasing degree of deformation, both the driving forces (increasing dislocation density and

**Table 13.6** Recrystallization mechanisms for AKS-W wires (after [13.17, 48, 49])

| Microstructural state | Processes |
|---|---|
| Evolution of the microstructure during wire drawing | ● Formation of a dislocation cell structure by static and dynamic recovery processes. |
| Coarsening of the microstructure during annealing | ● Annealing temperature 800–1400 °C:<br>– Reduction of the dislocation density within the cell walls<br>– Break-up of the K-containing stringers into pearl rows of bubbles<br>– Migration of longitudinal grain boundaries is strongly reduced by pearl rows of bubbles<br>– Similar ⟨110⟩ texture as in the as-worked state.<br>● For low heating rates, partial or even entire bubble rows can be dragged by the boundaries moving in the transverse direction. As a result, row/row collision and bubble coalescence can occur<br>● The temperature up to which the coarsened substructure remains stable depends on the degree of deformation (e.g., diameter 0.18 mm: 2100 °C/15 min). The coarsened substructure has a significant portion of high-angle grain boundaries (misorientation angles higher than 15°). |
| Exaggerated grain growth | Nucleation and growth of large interlocking grains occur by primary recrystallization, whereby a subgrain begins to grow laterally at the expense of neighboring polygonized subgrains:<br>● Because of the pearl row of bubbles, the rate of grain boundary movement is higher in the axial, than in the transverse direction<br>● Because of the interaction between the bubbles and the growing grains, the grain boundaries possess a wave-like, interlocking structure<br>● The grain aspect ratio of the recrystallized structure increases with increasing number of K bubbles. The number of K bubbles is a function of the K-content, the degree of deformation and the TMT<br>● Highly deformed, recrystallized wires reveal a ⟨531⟩ texture |

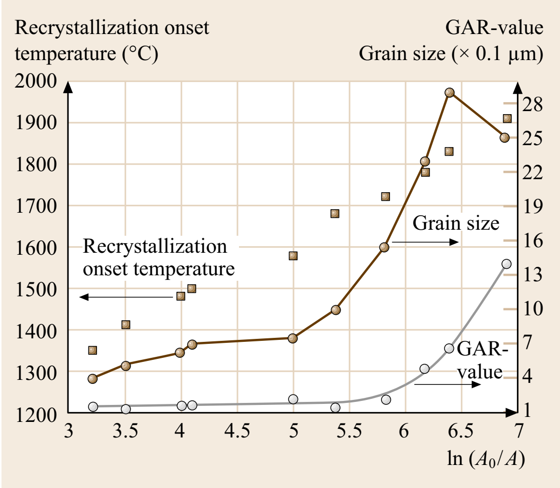


**Fig. 13.16** Recrystallization onset temperature, grain size, and grain aspect ratio (GAR) versus $\ln(A_0/A)$. AKS-W grade with K content of $42\,\mu g\,g^{-1}$; deformation temperature below the onset temperature of recrystallization; no intermediate heat treatments above recrystallization temperature; annealing time = 15 min; heating rate = $3\,K\,s^{-1}$; annealing atmosphere = hydrogen; annealing temperature for GAR evaluation = 2200 °C ($t_a = 5$ min); grain size measured in transverse direction (after [13.33]) ▶

low-angle/high-angle boundary volume) and dragging forces (increasing length of stringers of K-filled pores and, as a consequence, increasing number of K bubbles formed) become larger. During the first deformation steps the increase of the driving forces outweighs that of the dragging forces. Then the rise of the dragging forces starts to dominate, resulting in an increase of the recrystallization temperature (Fig. 13.16). With increasing length of the K stringers/number of K bubbles, the significance of the dragging effect in the transverse direction increases, resulting in an increase of the grain aspect ratio (GAR) in the recrystallized state. A marked increase of the GAR starts at a degree of deformation that coincides with a pronounced increase of the transverse grain size, as illustrated in Fig. 13.16.

## 13.4 Mechanical Properties

### 13.4.1 Influence of Thermomechanical Treatment (TMT) and Impurities

#### Mo and W Alloys [13.33]

The formation of a cellular dislocation structure increases both strength and fracture toughness [13.50, 51]. Additionally, the mechanical properties depend on the type of deformation process, purity, and heat treatment. The thermomechanical treatment (TMT) serves to obtain the specified shape, to eliminate the porosity, and to adjust the mechanical and structural properties. In particular, the evolution of the density distribution, pore size and shape, and its interaction with the mechanical properties are of high importance [13.17, 52–54].

During hot deformation which is usually the primary working step for both Mo and W, some investigators assume that high-angle grain boundaries are formed and migrate, grains are subdivided by low-angle boundaries, and new large-angle boundaries are formed by coarsening of the substructure [13.55]. Grains with an aspect ratio close to one and a low dislocation density are formed.

Following hot deformation, the material is processed at temperatures below the recrystallization onset temperature, but above the onset temperature of polygonization, leading to a cellular dislocation structure. The cell boundaries become impenetrable for slip dislocations and behave like grain boundaries, when the misorientation between neighboring cells is higher than a critical value of about 4° for Mo and W [13.50]. The formation of a misoriented cellular dislocation structure results both in an increase of strength and a decrease of the ductile–brittle transition temperature (DBTT). Both effects become more significant with increasing degree of deformation which results in a smaller effective grain size [13.50]. The size of the misoriented cellular dislocation structure depends sensitively on the deformation temperature. A high deformation temperature implies large grains [13.56]. Therefore it is essential to control the deformation temperature carefully. The control of the microstructure at intermediate steps has also been recommended [13.57].

The production yield is mainly decreased by the formation of grain boundary cracks. The cohesion of the grain boundaries is believed to be the controlling factor limiting the ductility of Mo and W [13.58]. Impurities segregated at the grain boundaries can lead to a strong decrease in ductility. Based on both semi-empirical and first principle modeling of the energetics and the electronic structures of impurities on a $\Sigma3(111)$ grain boundary in W, it was concluded that the impurities N, O, P, S, and Si weaken the intergranular cohesion, while B and C enhance the interatomic interaction across the grain boundary [13.58].

The amount of O in Mo ($\approx 10\,\mu g\,g^{-1}$) and W ($\approx 5\,\mu g\,g^{-1}$) is considered to be sufficient to form a monolayer of O on the grain boundaries as long as the grain size is not smaller than $10\,\mu m$. During recrystallization a migrating grain boundary can be saturated by collecting impurities while sweeping the volume. Based on the investigation of arc cast Mo samples, a beneficial effect of C was found and was attributed to following mechanisms [13.59]:

- Suppression of oxygen segregation
- Precipitation of carbides, acting as dislocation sources
- Formation of an epitaxial relationship between precipitates and bulk crystals at grain boundaries.

From these findings it was proposed that a C/O atomic ratio of $>2$ should improve the mechanical properties of Mo. The results obtained with arc-cast samples published in [13.59] could not be reproduced for samples produced by a P/M route [13.60].

As a consequence of the above mentioned effects, but in contrast to many other metallic materials, the fracture toughness of Mo and W is strongly reduced with increasing degree of recrystallization. With increasing plastic deformation, the fracture toughness increases (Sect. 13.4.4), combined with a transition from intercrystalline to transcrystalline cleavage and to a transcrystalline ductile fracture [13.51, 61, 62].

With increasing degree of deformation the working temperature can be progressively reduced. In particular, products with a high degree of deformation such as wires, thin sheets, and foils can be subjected to a high degree of deformation at a temperature below the polygonization temperature. The reduction of grain boundaries oriented transversely to the drawing direction increases the bending ductility of W [13.63]. W wire with an optimum ductility can only be obtained, when deformed in such a way that dynamic recovery processes occur without polygonization [13.64]. Other recovery phenomena, besides polygonization, are described in [13.65]. However a high degree of deformation below the onset temperature for dynamic polygonization favors the formation of longitudinal cracks.

Thin sheets and foils, annealed under conditions resulting in a small fraction of primarily recrystallized grains, can show a very specific fracture behavior, i. e., cracks running at an angle of 45° to the rolling direction [13.66, 67]. Such 45° embrittlement is caused by the nucleation of critical cracks at isolated grains formed by recrystallization of weak secondary components of the texture. Cracks propagate under 45° to the rolling direction owing to the alignment of the cleavage planes in the rolling texture [13.66].

### Nb and Ta Alloys

Contrary to Mo and W, pure Nb and Ta can be deformed at room temperature. Only highly-alloyed materials require breaking down the ingot microstructure either by forging or extrusion at elevated temperatures. In these cases the ingot has to be protected to prevent an interaction with the atmosphere. The mechanical behavior of pure annealed Nb and Ta is characterized by a high ductility and low work-hardening rate. The influence of deformation on the yield strength and fracture elongation of pure Ta is shown in Fig. 13.17.

Mechanical properties of Nb- and Ta-based alloys are strongly influenced by interstitial impurities, e.g., O, N, C, and H. The generally lower content of impurities and the larger grain size are the reasons why melt-processed Nb and Ta have a lower room-temperature tensile strength compared to sintered material. As an example, the influence of O on the mechanical properties of Ta is presented in Fig. 13.18.

After deformation both Nb- and Ta- based alloys are usually heat treated in high vacuum before delivering in order to achieve a fine grained primarily recrystallized microstructure.

## 13.4.2 Static Mechanical Properties

### Properties at Low Temperatures and Low Strain Rates

The flow stress of the transition metals Mo, W, Nb, and Ta is strongly dependent on temperature and strain

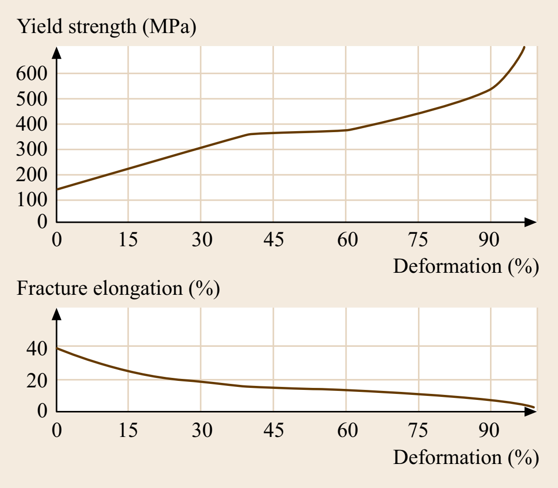


**Fig. 13.17** Yield strength and fracture elongation of Ta versus degree of deformation at room temperature (after [13.68])

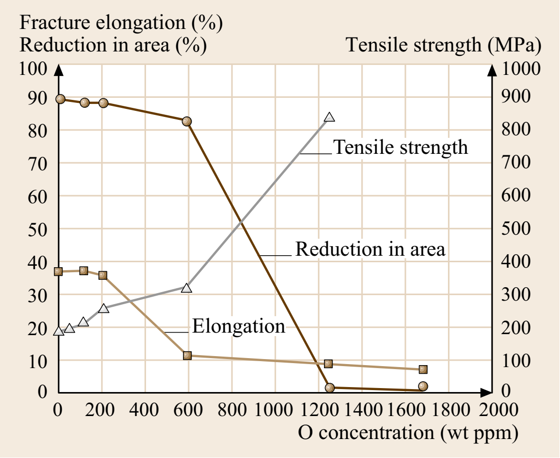


**Fig. 13.18** Tensile strength, fracture elongation, and reduction in area versus oxygen concentration of Ta specimens tested at room temperature (after [13.69])

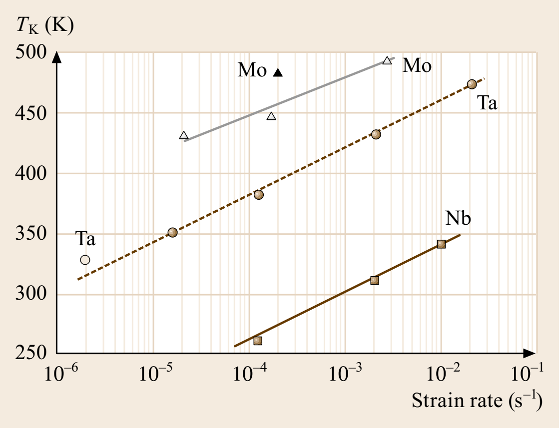


**Fig. 13.20** Dependence of $T_K$ on strain rate (after [13.72]) except for single values for Mo (*filled triangle*) (after [13.41]) and Ta (*open circle*) (after [13.41]). Those two values are not part of the fitted curve

rate below a characteristic transition temperature $T_K$ (knee temperature; corresponding to 0.1–0.2 of the absolute melting temperature) and plastic strain rates below $1 \times 10^{-5}\,s^{-1}$ [13.70]. As an example, experimental data on the temperature dependence of the flow stress of recrystallized Ta are shown in Fig. 13.19. This dependence has been attributed to the characteristic behavior of screw dislocations [13.71]. The transition temperature $T_K$ was shown to depend on the strain rate (Fig. 13.20) [13.41, 72].

For testing temperatures $T < T_K$ the flow stress increases markedly. Borderlines between elastic/anelastic

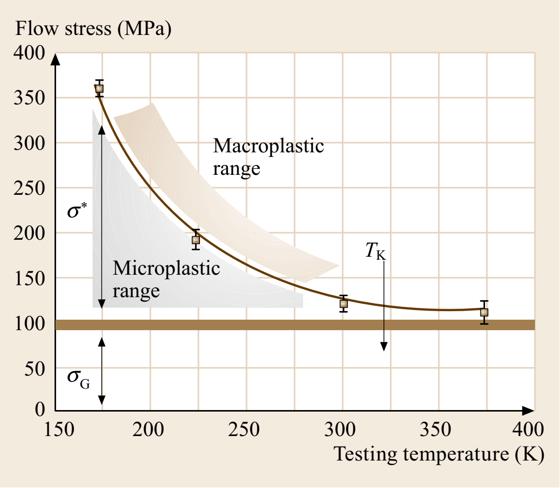


**Fig. 13.19** Temperature dependence of the flow stress (at $\varepsilon_{pl} = 1 \times 10^{-5}$) of recrystallized Ta under monotonic loading and $d\varepsilon/dt = 2 \times 10^{-6}\,s^{-1}$, $T_K$: *knee* temperature, $\sigma_G$: athermal range, $\sigma^*$: thermal range (after [13.41])

strain ($\sigma_A$) and microstrain/macrostrain deformation ranges can be deduced, subdivided into athermal ($\sigma_G$) and thermal ($\sigma^*$) ranges. The lower borderline of the microplastic region is almost independent of temperature and may be called the intrinsic flow stress which is much lower than the conventionally determined flow stress (technical flow stress). In the stress range between the intrinsic and the technical flow stress below $T_K$, strains of up to several percent were observed after extended loading times for Mo and Ta [13.73, 74]. The effect of temperature and strain rate on the monotonic microflow behavior of bcc metals as functions of temperature and strain rate was presented schematically [13.75]. Experimental data for Mo and Ta in constant load tests (low temperature creep tests) for stresses considerably below the technical flow stress are shown in Figs. 13.21 and 13.22. After a considerable incubation period, depending on the testing temperature and stress, a rapid increase in strain can be noticed approaching a saturation strain which depends on the stress level. The effect of the loading rate on the instantaneous plastic strain can be revealed with high resolution in loading–unloading tests under various constant loading rates [13.41, 74]. This microflow behavior may be significant for components at low temperatures and low stress levels, e.g., under storage conditions. Internal stresses in semi-finished products may be reduced even at room temperature to levels corresponding to the intrinsic flow stress [13.74].

A significant influence of the strain rate on the tensile properties at room temperature was determined for recrystallized Mo and Ta (Fig. 13.23) [13.41], in close agreement with literature data [13.76]. This strain rate effect makes it imperative for comparison of test data to list the test conditions.

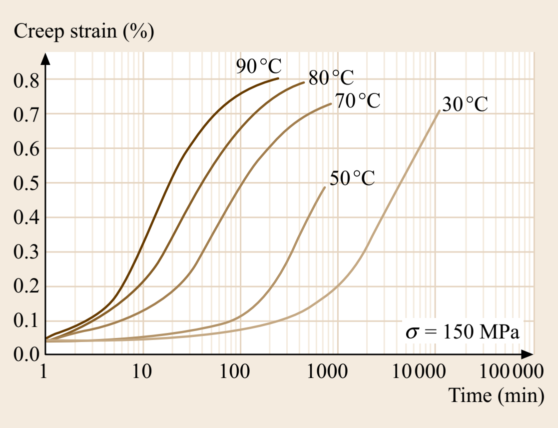


**Fig. 13.21** Creep strain of recrystallized Mo at $\sigma = 150\,\mathrm{MPa}$ for $30\,°\mathrm{C} \leq T \leq 90\,°\mathrm{C}$ (after [13.23])

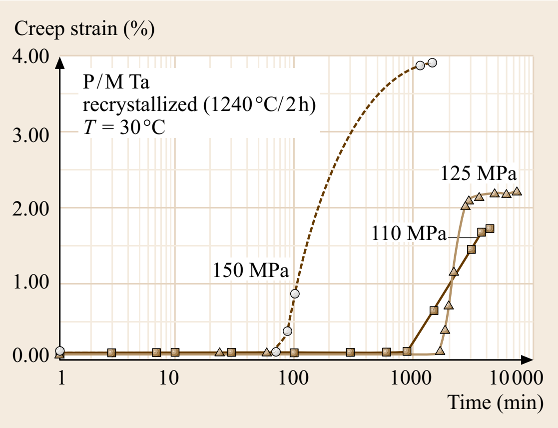


**Fig. 13.22** Creep elongation of recrystallized Ta sheets (thickness = 2 mm) at 30 °C for $110\,\mathrm{MPa} \leq \sigma \leq 150\,\mathrm{MPa}$ (after [13.23])

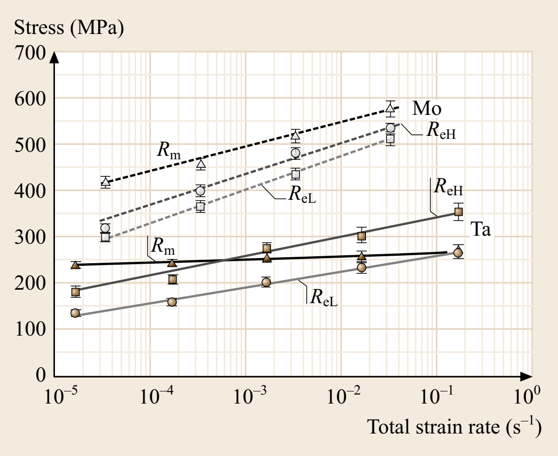


**Fig. 13.23** Effect of strain rate on tensile properties at room temperature of recrystallized Mo and recrystallized Ta (after [13.41])

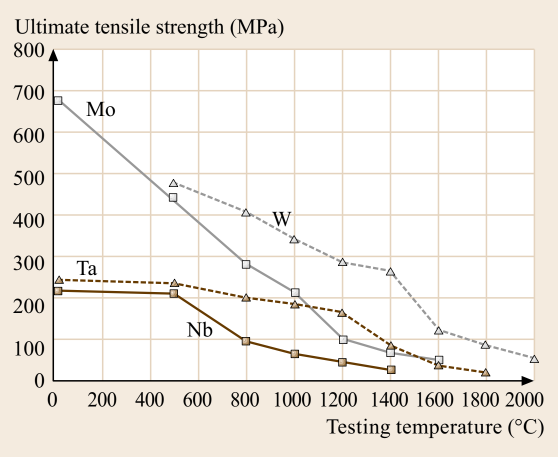


**Fig. 13.24** Ultimate tensile strength versus testing temperature for Mo, W, Ta, and Nb rods in their usual delivering condition. Mo, W: diameter = 25 mm (stress relieved); Ta, Nb: diameter = 12 mm (recrystallized); technical strain rates $= 1.0 \times 10^{-4}\,\mathrm{s}^{-1}$ up to the 0.2% yield strength followed by $3.3 \times 10^{-3}\,\mathrm{s}^{-1}$ (Mo, room temperature), $1.7 \times 10^{-3}\,\mathrm{s}^{-1}$ (Mo, elevated temperatures), $8.3 \times 10^{-4}\,\mathrm{s}^{-1}$ (W, elevated temperatures), $6.7 \times 10^{-4}\,\mathrm{s}^{-1}$ up to the 0.2% yield strength followed by $3.3 \times 10^{-3}\,\mathrm{s}^{-1}$ (Nb, Ta for all testing temperatures) (after [13.12])

### Properties at Elevated Temperatures

A rough ranking of the high temperature strength of Mo and W alloys can be obtained from the comparison presented in Table 13.5 (Sect. 13.3). Carbide-precipitation strengthened Mo-based alloys (MHC, TZM) and alloys high in Re (Mo-50 wt% Re, W-26 wt% Re) have the highest tensile strength. Alloys containing K (AKS-W, AKS-W-$ThO_2$) exhibit high strength only in the case of a high preceding plastic deformation.

A comparison of the high-temperature strength of rods made of Mo, W, Nb, and Ta in their usual state of delivery is given in Fig. 13.24. The usual state of delivery for Mo is stress-relieved with a highly polygonized microstructure with up to 5% recrystallized grains. W is usually delivered in the as worked state.

The decrease of tensile strength and the increase of reduction in area with increasing testing temperature can be related to changes in the fracture mode (Fig. 13.25), i. e., cleavage fracture, brittle grain boundary failure, and ductile transcrystalline failure [13.61].

The influence of alloying Ta with W is illustrated in Fig. 13.26 for Ta2.5W and Ta10W, which are the main commercial Ta-based alloys. Figure 13.27 summarizes values of $R_{p0.2}$ of the most common Nb-based

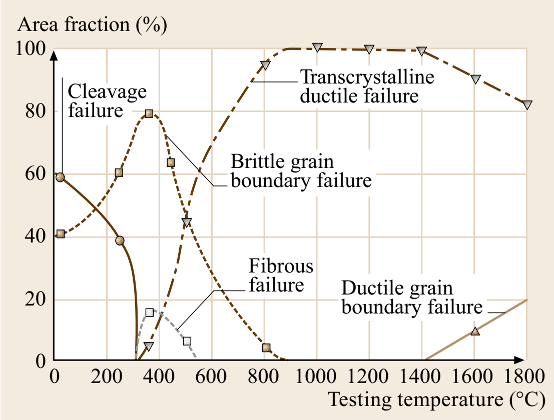


**Fig. 13.25** Effect of testing temperature on fracture modes of pure W, stress relieved at 1000 °C/6 h (after [13.61])

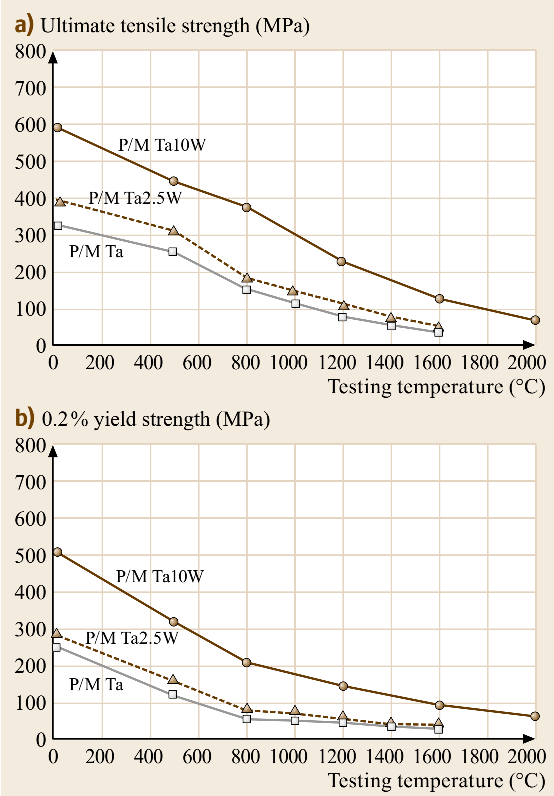


**Fig. 13.26a,b** The ultimate tensile strength $R_m$ **(a)** and the yield strength $R_{p0.2}$ **(b)** versus testing temperature of P/M Ta, P/M Ta2.5W, and P/M Ta10W sheets that are 1 mm thick, with impurity content ($\mu g\, g^{-1}$) Ta: O = 60, N = 10, H = 1.8, C < 5; Ta2.5W: O = 70, N = 12, H = 2.4, C = 5; Ta10W: O = 31, N < 5, H < 1, C = 21; material condition = recrystallized, technical strain rates $= 6.7\times10^{-4}\,s^{-1}$ up to $R_{p0.2}$, followed by $3.3\times10^{-3}\,s^{-1}$ (after [13.23])

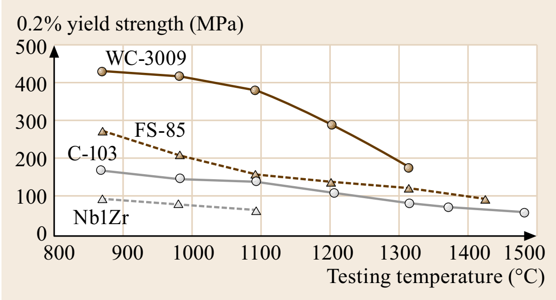


**Fig. 13.27** Effect of testing temperature on $R_{p0.2}$ for common Nb-based alloys (after [13.77])

alloys at elevated temperatures. All of these alloys are hardened primarily by solid solution strengthening; however, small amounts of precipitates are present.

For comparison, the high-temperature strength of stress-relieved 1 mm sheets made of Mo- and W-based materials is shown in Fig. 13.28. For short-term application under high stresses, the precipitation strengthened Mo alloys TZM and MHC offer the best performance up to a service temperature of 1500 °C. For higher temperatures, W-based materials should be applied. Ta-based alloys are used only if additional high ductility is required after cooling to room temperature.

## 13.4.3 Dynamic Properties

### Microplasticity Effects Under Cyclic Loading at Low Temperatures

Microplasticity effects under monotonic loading have been reported in the literature for single and polycrystalline Mo and Ta [13.75, 78]; information regarding the effects of strain rate and temperature on the cyclic stress–strain response is given in [13.41, 74]. Most experiments on cyclic stress–strain behavior have been carried out at room temperature. When bcc metals are deformed at $T < 0.2T_m$, microstrain ($\varepsilon_{pl} < 10^{-3}$) is characterized as the plastic strain, accommodated by the motion of non-screw dislocations [13.71, 73]. These differences are manifested in the temperature and strain-rate dependence of the flow behavior [13.75, 79]. Investigations of Mo and Ta showed that a true microplastic deformation can only be considered at plastic strains of less than $5\times10^{-4}$ [13.41]. The critical temperature below which the marked increase in the cyclic flow stress occurs is in the range of 25–80 °C for Ta and between 200 and 280 °C for Mo, depending on the strain rate. The experimental results for Ta showed that the highest cyclic plastic strains are obtained under strain rates between $1\times10^{-8}$ and $2\times10^{-6}\,s^{-1}$. As an example, the effect of the loading rate on the cyclic plastic strain of recrystallized Ta during tension–compression cycles at loading rates between

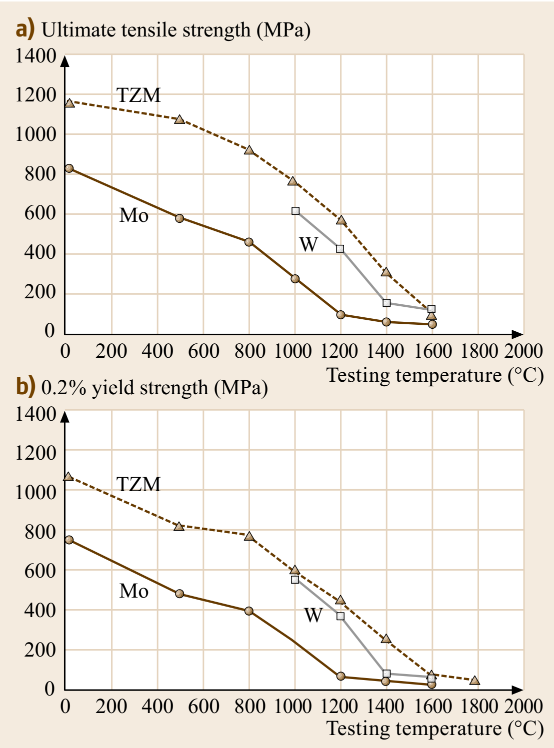


**Fig. 13.28a,b** The ultimate tensile strength $R_m$ **(a)** and the yield strength $R_{p0.2}$ **(b)** versus testing temperature for Mo, TZM, and W sheets that are 1 mm thick. Material condition = stress relieved, technical strain rates $= 2.0 \times 10^{-3}\,s^{-1}$ (Mo, TZM, room temperature), $1.3 \times 10^{-3}\,s^{-1}$ (Mo, TZM, elevated temperatures), $3.3 \times 10^{-4}\,s^{-1}$ up to $R_{p0.2}$, followed by $6.7 \times 10^{-4}\,s^{-1}$ (W, elevated temperatures) (after [13.23]) ◄

$0.042\,MPa\,s^{-1}$ (duration of one cycle = 190 min) and $4.2\,MPa\,s^{-1}$ (duration of one cycle = 1.9 min) is shown in Fig. 13.29 [13.41].

### High-Cycle Fatigue Properties

Most fatigue data are reported in form of stress versus number of cycles to failure ($S-N$) curves. For Mo a fatigue limit may be approached for $N > 10^7$ under stress-controlled conditions [13.80]. Experiments were conducted at test frequencies up to 20 kHz. The results of such tests should be considered with caution, taking into account the temperature and strain-rate sensitivity of bcc metals. Representative $S$–$N$ curves for as-worked and recrystallized Mo, and a comparison of push–pull- and bending–fatigue-tested Mo sheet specimens are shown in Figs. 13.30 [13.23] and 13.31 [13.23].

The reported fatigue test data for various test methods are summarized in Table 13.7 with the fatigue limit ($S_e$) and the ratio of fatigue limit to tensile–stress ($S_e/R_m$) as characteristic parameters. Methods of statistical evaluation of test data were published [13.80, 81]. A decrease in fatigue limit with decreasing cyclic frequency was found.

Cyclic hardening/softening was deduced and cyclic stress–strain curves over wide ranges of plastic strain amplitudes were published in [13.82, 83] for Mo, in [13.76, 84, 85] for Ta, and in [13.86] for Nb and Nb1Zr. Cyclic stress–plastic-strain curves are given in Figs. 13.32 and 13.33 for Mo and Ta at various testing temperatures. The ranges of microplastic and macroplastic strain can be differentiated, based on the different slopes of the curves.

The elevated temperature fatigue behavior of TZM was investigated for testing temperatures between 300 and 500 °C [13.89]. Brittle failure under high cycle fatigue conditions was found over the entire temperature range, with a significant decrease in fatigue strength with increasing temperature.

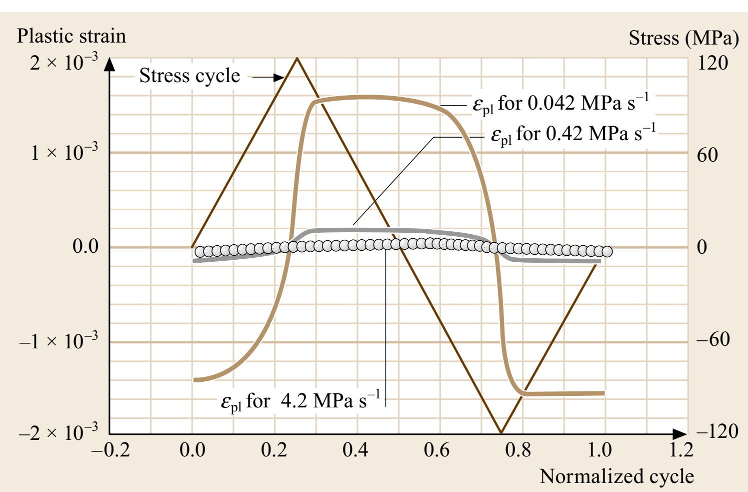


**Fig. 13.29** Effect of loading rate on cyclic plastic strain of recrystallized Ta during a tension–compression cycle ($R = -1$). Stress amplitude = 120 MPa; testing temperature = 25 °C; duration of a cycle at $0.042\,MPa\,s^{-1}$ = 190 min, at $4.2\,MPa\,s^{-1}$ = 1.9 min; maximum plastic strain rate at all loading rates $\approx 3 \times 10^{-6}\,s^{-1}$ (after [13.41])

**Table 13.7** Summary of fatigue data of refractory metals, pretreatment: Aw: as worked, Sr: stress relieved, Rxx: recrystallized, RT: room temperature

| Material | Production process | Dimension (mm) (plate: thickness, bar: diameter) | Pretreatment $T$ (°C)/$t_a$ (h) | | Test temperature, test frequency | $S_e$ (MPa) | $S_e/R_m$ | Reference |
|---|---|---|---|---|---|---|---|---|
| **Rotating bending fatigue, $R = -1$, fatigue limit $S_e$ for 50% probability at $N = 5 \times 10^7$** | | | | | | | | |
| Mo | P/M | Bar 12 | Aw | | RT, 100 Hz | 450 | 0.68 | [13.23] |
| | | | Rxx | 1200/1 | RT, 100 Hz | 220 | 0.44 | |
| Mo5Re | P/M | Bar 12 | Aw | | RT, 100 Hz | 450 | 0.68 | [13.23] |
| | | | Sr | 900/6 | RT, 100 Hz | 400 | 0.68 | |
| | | | Rxx | 1300/1 | RT, 100 Hz | 230 | 0.48 | |
| Mo41Re | P/M | Bar 12 | Aw | | RT, 100 Hz | 690 | 0.62 | [13.23] |
| | | | Sr | 1050/6 | RT, 100 Hz | 620 | | |
| | | | Rxx | 1400/1 | RT, 100 Hz | 320 | 0.36 | |
| TZM | P/M | Bar 12 | Aw | | RT, 100 Hz | 550 | 0.62 | [13.23] |
| | | | Sr | | RT, 100 Hz | 560 | | |
| | | | Rxx | 1500/1 | RT, 100 Hz | 340 | 0.57 | |
| W | P/M | Bar 12 | Aw | | RT, 100 Hz | 760 | 0.48 | [13.23] |
| | | | Rxx | 1600/1 | RT, 100 Hz | 310 | 0.70 | |
| W5Re | P/M | Bar 12 | Aw | | RT, 100 Hz | 770 | 0.71 | [13.23] |
| | | | Rxx | 1800/1 | RT, 100 Hz | 440 | 0.65 | |
| W26Re | P/M | Bar 12 | Aw | | RT, 100 Hz | 820 | 0.54 | [13.23] |
| | | | Rxx | 1700/1 | RT, 100 Hz | 450 | 0.39 | |
| $W2ThO_2$ | P/M | Bar 12 | Rxx | 1900/1 | RT, 100 Hz | 365 | 0.64 | [13.23] |
| Nb | P/M | Bar 5.9 | Aw | | RT, 100 Hz | 225 | 0.42 | [13.87] |
| | | | Rxx | | RT, 100 Hz | 220 | 0.51 | |
| Ta | P/M | Bar 5.9 | Aw | | RT, 100 Hz | 290 | 0.92 | [13.87] |
| | | | Rxx | | RT, 100 Hz | 270 | 0.95 | |
| **Push–pull fatigue, $R = -1$, fatigue limit $S_e$ for $N = 1 \times 10^7$** | | | | | | | | |
| Mo | P/M | Plate 1 | Rxx | 1200/1 | RT, 0.05 Hz | 195 | | [13.83] |
| TZM | P/M | Bar 50 | Aw | | RT, 25 Hz | 440 | | [13.88] |
| | | | Aw | | 850 °C, 25 Hz | 250 | | |
| Ta | | Plate 2 | Aw | | RT, 0.05 Hz | 205 | | [13.83] |
| | | | Aw | | RT, 10 Hz | 225 | | |
| | | | Rxx | 1200/2 | RT, 0.05 Hz | 180 | | |
| | | | Rxx | 1200/2 | RT, 10 Hz | 210 | | |
| **Bending fatigue, $R = -1$, fatigue limit $S_e$ for 50% fracture probability at $N = 1 \times 10^7$** | | | | | | | | |
| Mo | P/M | Plate 2 | Aw | | RT, 25 Hz | 520 | | [13.23] |
| | | | Sr | 780/6 | RT, 25 Hz | 540 | | |
| | | | Rxx | 1200/1 | RT, 25 Hz | 280 | | |
| Mo5Re | P/M | Plate 1.6 | Sr | | RT, 25 Hz | 460 | 0.56 | [13.23] |
| Mo41Re | P/M | Plate 1.6 | Sr | | RT, 25 Hz | 680 | 0.61 | [13.23] |
| TZM | P/M | Plate 2 | Aw | | RT, 25 Hz | 650 | | [13.23] |
| | | | Sr | 1150/6 | RT, 25 Hz | 650 | | |
| | | | Rxx | 1500/1 | RT, 25 Hz | 460 | | |
| W | P/M | Plate 2 | Aw | | RT, 25 Hz | 520 | | [13.23] |
| | | | Rxx | 1600/1 | RT, 25 Hz | 225 | | |
| Ta | P/M | Plate 1 | Aw | | RT, 25 Hz | 335 | 0.56 | [13.23] |
| | | | Rxx | 1200/1 | RT, 25 Hz | 240 | 0.75 | |
| Ta | EB | Plate 1 | Aw | | RT, 25 Hz | 270 | 0.61 | [13.23] |
| | | | Rxx | 1200/1 | RT, 25 Hz | 220 | 0.96 | |
| Ta2.5W | P/M | Plate 1 | Rxx | 1300/1 | RT, 25 Hz | 310 | 0.79 | [13.23] |
| Ta2.5W | EB | Plate 1 | Rxx | 1300/1 | RT, 25 Hz | 270 | 0.69 | [13.23] |
| Ta10W | EB | Plate 0.64 | Aw | | RT, 25 Hz | 480 | | [13.69] |

**Table 13.7** (continued)

| Material | Production process | Dimension (mm) (plate: thickness, bar: diameter) | Pretreatment $T$ (°C)/$t_a$ (h) | | Test temperature, test frequency | $S_e$ (MPa) | $S_e/R_m$ | Reference |
|---|---|---|---|---|---|---|---|---|
| **High-frequency push–pull fatigue, $R = -1$, fatigue limit $S_e$ for 50% fracture probability at $N = 10^8$** | | | | | | | | |
| Mo | P/M | Bar 11 | Rxx | 1300/4 | RT, 20 kHz | 278 | 0.56 | [13.80] |
| TZM | P/M | Bar 11 | Rxx | 1600/2 | RT, 20 kHz | 383 | 0.69 | [13.80] |
| Ta | EB | Bar 3 | Aw | | RT, 20 kHz | 383 | 0.72 | [13.23] |
| | | | Sr | | RT, 20 kHz | 286 | 0.92 | |
| Ta2.5W | P/M | Plate 2 | Rxx | | RT, 20 kHz | 300 | | [13.23] |
| Ta10W | P/M | Bar 12 | Rxx | | RT, 20 kHz | 580 | | [13.23] |
| Nb | | Bar 3 | Aw | | RT, 20 kHz | 230 | 0.80 | [13.81] |
| | | | Rxx | | RT, 20 kHz | 220 | 0.65 | |

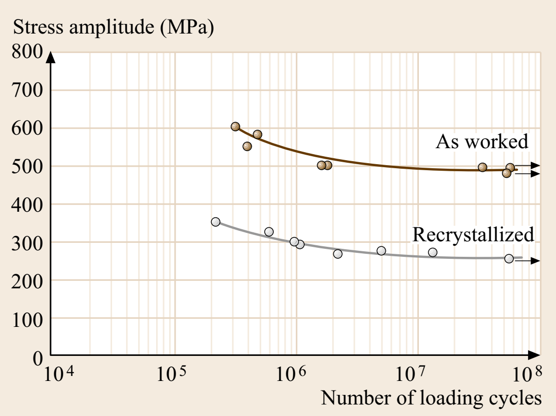


**Fig. 13.30** Rotating–bending fatigue test results for as worked and recrystallized Mo rods (diameter = 25 mm) at room temperature (after [13.23])

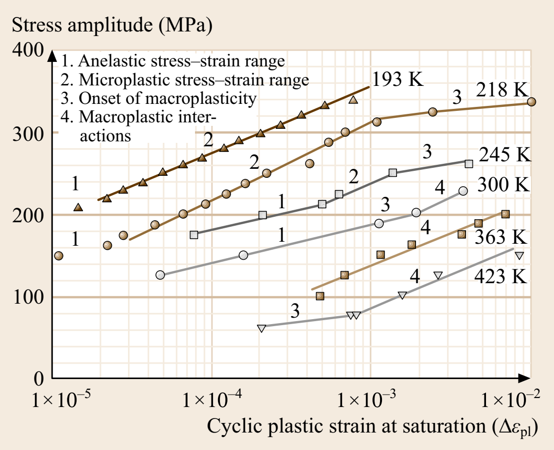


**Fig. 13.32** Cyclic-stress–plastic-strain curves of recrystallized Mo at different temperatures at a loading rate of 60 MPa s$^{-1}$ (after [13.41])

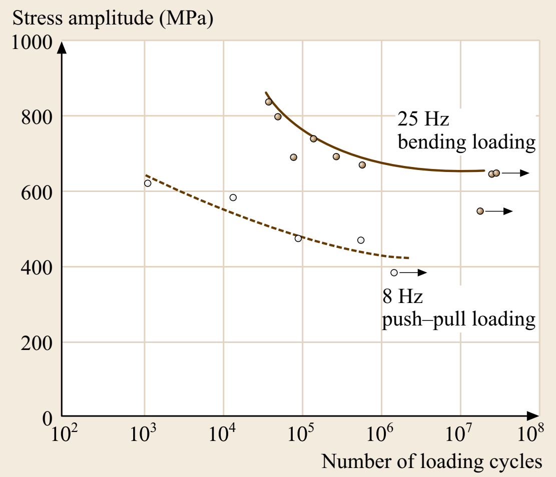


**Fig. 13.31** Comparison of test results of bending (at 25 Hz) and push–pull fatigue (at 8 Hz) tests of stress-relieved Mo sheet specimens (800 °C/6 h) (after [13.23]) at room temperature

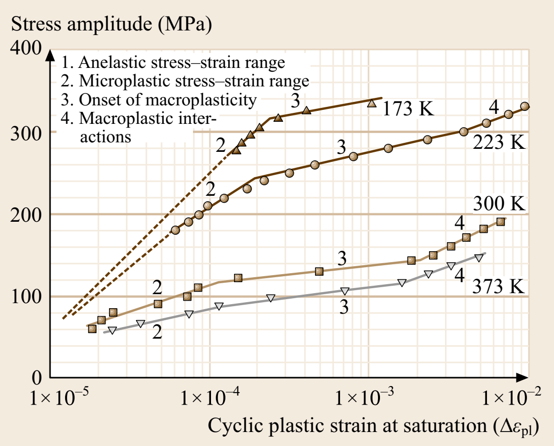


**Fig. 13.33** Cyclic-stress–plastic-strain curves of recrystallized Ta at different temperatures at a loading rate of 0.42 MPa s$^{-1}$ (after [13.41])

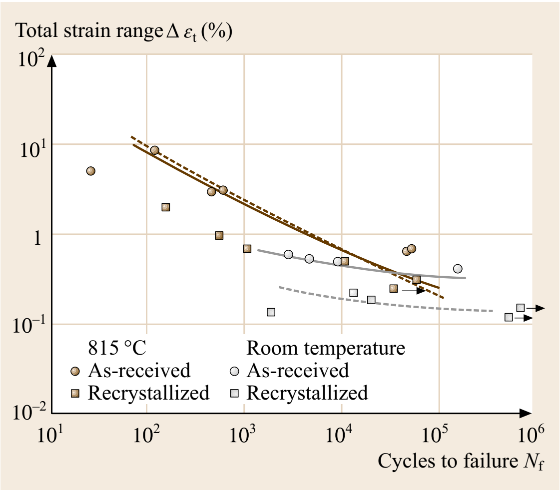


**Fig. 13.34** Low-cycle fatigue data of as-received and recrystallized W at room temperature and 815 °C (after [13.92])

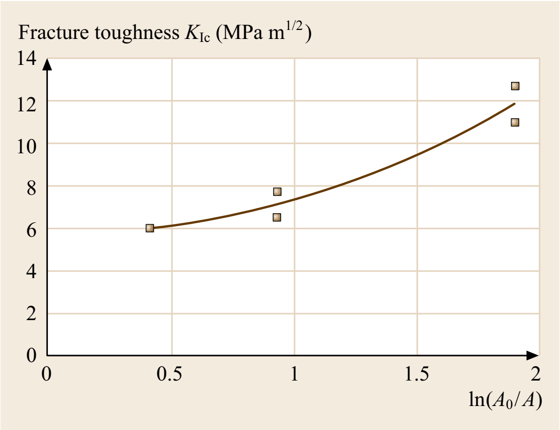


**Fig. 13.35** $K_{Ic}$ of forged Mo rods versus $\ln(A_0/A)$ (after [13.51])

### Low-Cycle Fatigue Properties

Results of low-cycle fatigue experiments under strain control on as worked W plate material at 815 °C are shown in Fig. 13.34. Low-cycle fatigue tests of pure W were performed in the temperature range between 1650 and 3300 °C [13.90]. A relationship $N_{failure} \approx \exp(-\alpha T)$ was found to be valid up to testing temperatures of 2700 °C [13.91]. In all cases the failure mode was intercrystalline. Similar results were also obtained at a testing temperature of 1232 °C [13.92]. The deformation behavior of Nb and Nb1Zr under plastic-strain control at room temperature was investigated and cyclic stress–strain curves published [13.86].

Low-cycle fatigue test data of Mo at high testing temperatures were reported in [13.93]. The influence of

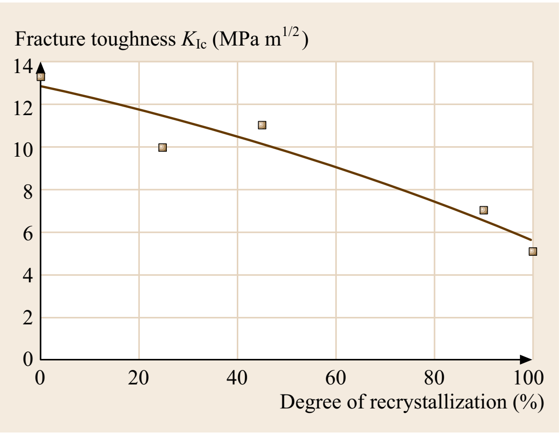


**Fig. 13.36** $K_{Ic}$ of forged Mo rods ($\varphi = 74\%$) versus degree of recrystallization (after [13.51])

microstructural changes in cold-worked Mo on the low-cycle fatigue behavior was reported for testing temperatures between 300 and 950 °C [13.94]. Deformation experiments under low-cycle fatigue conditions between room temperature and 100 °C showed that recrystallized Mo, in spite of the low temperature and stress level, exhibits considerable plastic strains which depend sensitively on the loading frequency [13.95]. Data on the high temperature (350 and 500 °C) isothermal mechanical fatigue behavior of TZM were reported and a model for lifetime prediction was proposed [13.89].

## 13.4.4 Fracture Mechanics Properties

### Fracture Toughness

Fracture toughness properties are affected by many parameters (processing route, thermomechanical pretreatments, microstructure, specimen and crack plane orientation; testing procedures as well as the preparation of the starting notch and of the fatigue precrack). Fracture toughness data for low carbon arc cast Mo and arc cast TZM plates have been published for testing temperatures between room temperature and 300 °C. At room temperature $K_{Ic}$-values between 15 and 22 MPa m$^{1/2}$ for both materials were found, while at 300 °C $K_{Ic}$-values of 64 MPa m$^{1/2}$ for Mo and 91 MPa m$^{1/2}$ for TZM were obtained [13.96]. Fracture toughness data for P/M TZM and P/M Mo-La-oxid plate materials have been presented in [13.97] for testing temperatures between −150 and 450 °C. For TZM a transition from low fracture toughness values (5.8 MPa m$^{1/2}$) to values > 30 MPa m$^{1/2}$ occurred at temperatures about 100 °C in the longitudinal direction and at 150 °C in the transverse direction. For the Mo-La-oxide material in the longituinal direction no transition to low fracture toughness values was observed at temperatures above

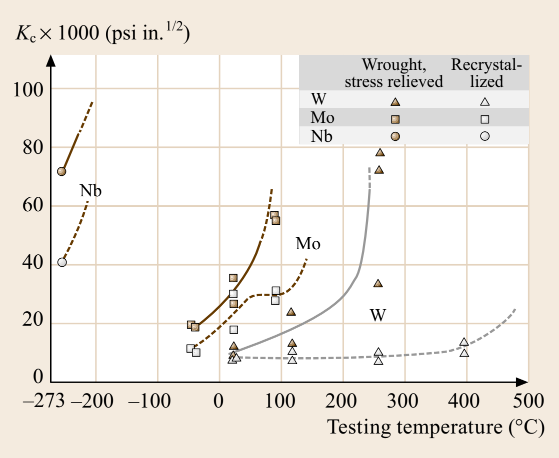


**Fig. 13.37** Effect of testing temperature on fracture toughness of unalloyed W, Mo, and Nb sheet specimens (after [13.100])

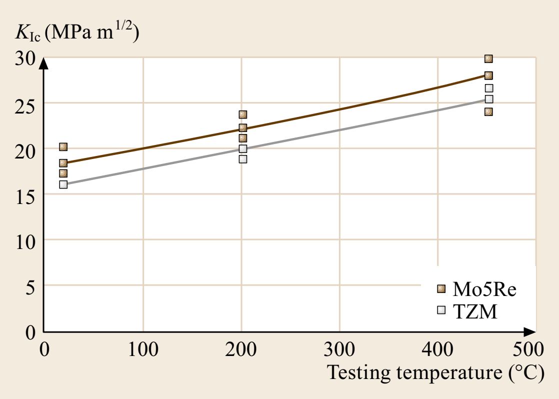


**Fig. 13.38** Effect of testing temperature on static fracture toughness of TZM and Mo5Re specimens (after [13.101])

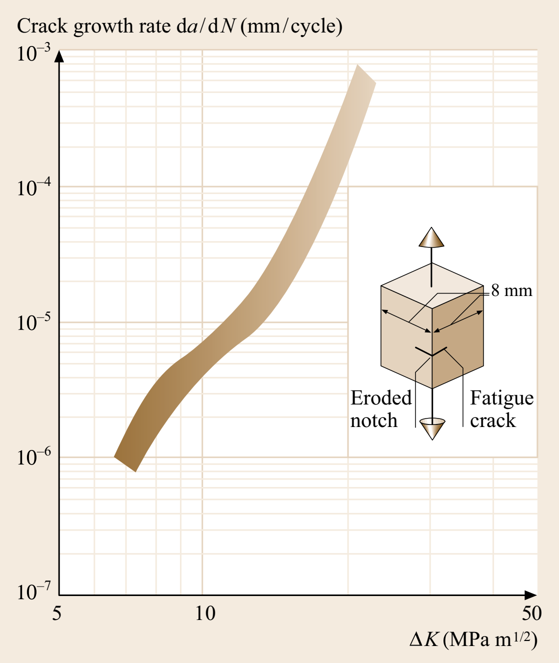


**Fig. 13.39** Crack propagation behavior of recrystallized P/M Ta10W specimens at room temperature at a stress ratio of $R = 0.4$ (after [13.109])

−150 °C while for the transverse direction a transition was found at room temperature.

Due to the peculiarities of the P/M production process, it is frequently not possible to introduce sufficient deformation into products of larger dimension in order to completely eliminate sinter pores which may affect the dynamic properties. The increase of fracture toughness with increasing degree of hot working of disc-shaped compact tension specimens, cut from a hot forged Mo bar is shown in Fig. 13.35 and the decrease of fracture toughness with increasing fraction of recrystallized microstructure in Fig. 13.36 [13.51].

Fracture toughness tests of polycrystalline W, W-$La_2O_3$ and AKS-W have shown the effect of grain size, texture, composition, grain boundary segregation and dislocation density below the DBTT [13.98, 99]. Fracture toughness data for Mo, TZM, and W materials are summarized in Table 13.8. Data taken at elevated temperature for Mo and W are shown in Fig. 13.37 [13.100], and for TZM in Fig. 13.38 [13.101]. Data for Nb could only be determined below −200 °C [13.100]. Data on the impact and dynamic toughness of Nb between −196 and 25 °C were reported in [13.102]. The dynamic cleavage fracture toughness was shown to be 37 MPa m$^{1/2}$, relatively independent on grain size and testing temperature.

### Fatigue Crack Growth

Few data on the linear region of crack growth were published for Ta10W (Fig. 13.39), and a Nb-W-Zr alloy [13.109, 110].

### Threshold Stress Intensity for Fatigue Crack Growth

The fatigue crack growth behavior of Mo, TZM, and W in the region near the threshold stress intensity, $\Delta K_{th}$, considered to correspond to fatigue crack growth rates of $da/dN < 10^{-13}$ m/cycle, is shown in Fig. 13.40 [13.23]. The available crack growth and threshold data are included in Table 13.9. An effective threshold value for fatigue crack growth, $\Delta K_{th,eff}$, can be computed. Methods for the determination of this effective threshold stress intensity range are described in [13.104]. The available data on $\Delta K_{th,eff}$ of Mo and TZM are listed in Table 13.9.

**Table 13.8** Fracture mechanical data for various refractory metals, pretreatment: Aw: as worked, Sr: stress relieved, Rxx: recrystallized, RT: room temperature. Specimen types: CT – compact tension, SCT –center surface cracked tension, DCT –disk-shaped compact tension, SNB –side notched bend, CNT –center through-thickness notched tension

| Material | Production process | Dimension (mm) (plate: thickness, bar: diameter) | Pretreatment $T$ (°C)/$t_a$ (h) | | Specimen type | Crack plane ASTM 399 | Test temperature | Fracture toughness (MPa m$^{1/2}$) | Reference |
|---|---|---|---|---|---|---|---|---|---|
| Mo | P/M | Plate 6.5 | Rxx | 1300/2 | CNT | L-T | RT | 9.5 | [13.23] |
| Mo | P/M | Bar 50 | Sintered | | DCT | R-C | RT | 6 | [13.51] |
| | | | Hot forged | | DCT | R-C | RT | 12 | |
| | | | Rxx | 1400/2 | DCT | R-C | RT | 5 | |
| Mo | VAC | Plate 6.4 | Sr | | CT | L-T/T-L | RT | 20/21 | [13.96] |
| | | | Rxx | | CT | L-T/T-L | RT | 18/19 | |
| | | | Sr | | CT | L-T/T-L | 300 °C | 74/70 | |
| | | | Rxx | | CT | L-T/T-L | 300 °C | 60/67 | |
| Mo5Re | | Bar 54 | Rxx | 1300/1 | DCT | R-C | RT/450 °C | 18/27 | [13.101] |
| Mo-0.3 wt% $La_2O_3$ | P/M | Plate | Sintered | | CT | L-T | RT | 25 | [13.103] |
| TZM | VAC | Plate 6.4 | Sr | | CT | T-L/L-T | RT | 19/15 | [13.96] |
| | | | Rxx | | CT | T-L/L-T | RT | 15/18 | |
| | | | Sr | | CT | T-L/L-T | 300 °C | 85/89 | |
| | | | Rxx | | CT | T-L/L-T | 300 °C | 59/68 | |
| TZM | P/M | Bar 54 | Aw | | DCT | R-C | RT | 19 | [13.62, 104] |
| | | Machined to 12 | Aw | | SCT | L-C | RT | 37 | |
| | | Swaged to 12 | Rxx | 1400/2 | SCT | L-C | RT | 19 | |
| W | | Bar 10 | | | SNB | C-R/L-R | −196 °C | 11/6 | [13.105] |
| | | | | | SNB | C-R/L-R | RT | 13/8 | |
| W | | Bar 25 | Aw | | SNB | R-L | RT/150 °C/ 300 °C/500 °C | 9/10/13/14 | [13.106] |
| W | Single crystal | Bar 16 (111)[011] | | | SNB | | −196 °C/RT | 9/31 | [13.105] |
| | | Bar 16 (011)[100] | | | SNB | | −196 °C/RT | 4/20 | |
| | | Bar 16 (100)[001] | | | SNB | | −196 °C/RT | 3/9 | |
| W | | | Aw | | SNB | | RT/400/600/ 800 | 15/21/26/39 | [13.107] |
| W5Re | | | Aw | | SNB | | RT/400 °C/ 600 °C | 11/26/58 | [13.107] |
| W-1 wt% $La_2O_3$ | P/M | Bar 25 | Aw | | SNB | R-L | RT/150 °C/ 300 °C/500 °C | 9/10/11/13 | [13.106] |
| Nb | | Plate 1.25 | Sr | | CNT | L-T | −253 °C | 40 | [13.100] |
| | | | Rxx | | CNT | L-T | −253 °C | 72 | |
| Nb | | | Rxx | | SNB | | −196 °C | 37 | [13.102] |
| | | | Rxx | | SNB | | RT | 37 | |

### Short Fatigue Crack Growth Behavior

The nucleation and growth behavior of short fatigue cracks is of considerable practical and theoretical significance. Differences in the growth behavior exist between initial short cracks (length comparable with microstructural features) and long cracks of macroscopic dimensions. The irregular growth rate of such short cracks (Fig. 13.41) may pose problems for a conservative prediction of fatigue life [13.108]. Microscopic observations during fatigue exposure of specimens, loaded at stress amplitudes slightly above the fatigue limit, show initially a surface deformation very early in fatigue life, followed by short crack initiation and growth up to the final long crack growth. The number of fatigue cycles of the various stages depends on the microstructure and the presence of second phase particles (Fig. 13.42) [13.111].

**Fig. 13.41a,b** Growth behavior of short surface cracks at room temperature ($R = -1$ and 20 kHz cyclic frequency) in a TZM specimen, tested at a stress amplitude of 375 MPa (after [13.108, 111]). **(a)** Crack length as function of number of loading cycles. **(b)** Crack growth rate as function of crack length ►

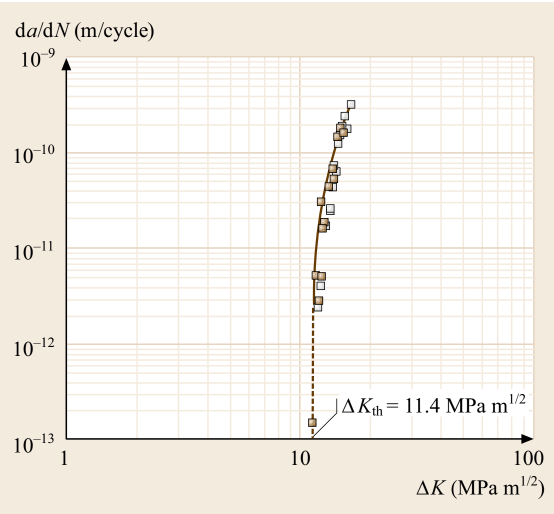


**Fig. 13.40** Crack growth curve near threshold stress intensity of a center surface cracked specimen machined from a recrystallized Mo5Re rod, tested at a stress ratio of $R = -1$, test temperature $= 50\,°C$, and 20 kHz cyclic frequency; *open symbols*: test under increasing load, *solid symbols*: tests under decreasing load (after [13.23])

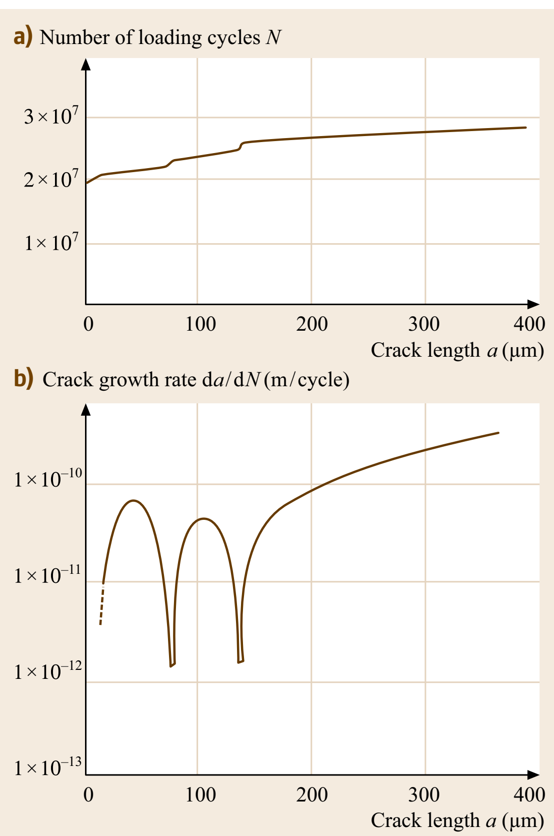


**Table 13.9** Fatigue crack growth and threshold data for various refractory metals, pretreatment: Aw: as worked, Sr: stress relieved, Rxx: recrystallized. RT: room temperature. Specimen types: CNT: center through-thickness notched tension, SCT: center surface cracked tension, SNT: side notched tension

| Material | Production process | Dimension (mm) (plate: thickness, bar: diameter) | Pretreatment | $T$ (°C)/$t_a$ (h) | Specimen type | Crack plane ASTM 399 | Test temperature, test frequency[a] | Stress ratio $R$ | d$a$/d$N$-range, (m/cycle) | $\Delta K_{th}^{b}$ | $\Delta K_{th,eff}^{c}$ | ASTM | Reference |
|---|---|---|---|---|---|---|---|---|---|---|---|---|---|
| Mo | P/M | Plate 6.5 | Rxx | 1300/2 | CNT | L-T | RT, 20 kHz | −1 | $10^{-13}$–$10^{-9}$ | 5.8 | | E647 | [13.23] |
| Mo | P/M | Bar 12 | Aw | | SCT | L-C | RT, 20 kHz | −1 | $10^{-13}$–$10^{-9}$ | 11.3 | 11 | E647 | [13.62] |
| | | | Rxx | 1400/2 | | | | | | 10.7 | 11 | | |
| Mo | P/M | Bar 12 | Sr | 850/1 | SNT | C-R | RT, 20 kHz | −1 | $10^{-13}$–$10^{-9}$ | 10.3 | 7.0 | E647 | [13.108] |
| | | | Rxx | 1400/2 | | | | | | 8.5 | 6.6 | | |
| TZM | P/M | Bar 12 | Rxx | 1700/2 | SNT | C-R | RT, 20 kHz | −1 | $10^{-13}$–$10^{-9}$ | 10.1 | 6.3 | E647 | [13.108] |
| Mo5Re | P/M | Bar 12 | Rxx | 1300/1 | SCT | L-C | RT, 20 kHz | −1 | $10^{-13}$–$10^{-9}$ | 11.4 | 9.9 | E647 | [13.23] |

[a] 20 kHz resonance test method, crack growth monitored by traveling light microscope
[b] $\Delta K_{th}$ corresponding to a crack growth rate of d$a$/d$N < 10^{-13}$ m/cycle
[c] $\Delta K_{th,eff}$ calculated from crack closure measurements based on strain gauge method

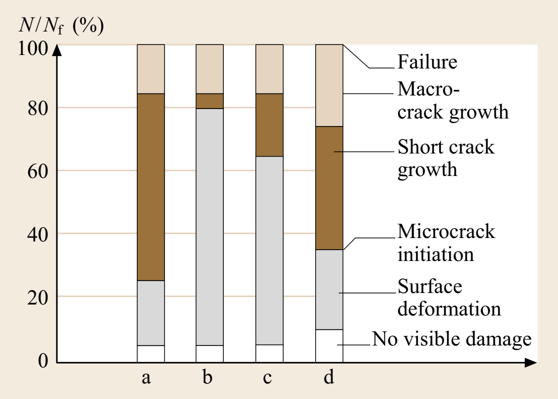


**Fig. 13.42** Fraction of total fatigue life spent on damage accumulation and crack growth in specimens of stress relieved Mo (a), recrystallized Mo (b), TZM with fine particles (c), and TZM with coarse particles (d) (after [13.111])

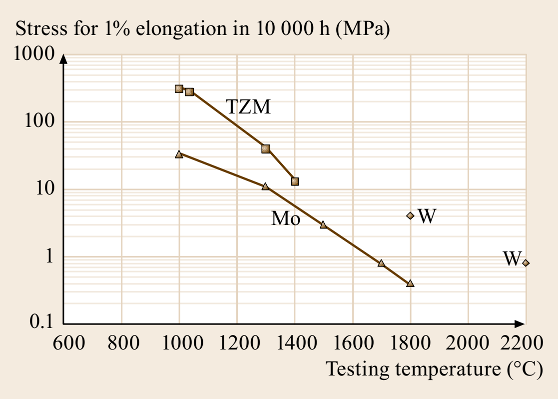


**Fig. 13.44** Comparison of 10 000 h/1% creep data for Mo, TZM, and W (after [13.1])

It is known that fatigue failures occur in defect containing materials after a high number of loading cycles ($N > 10^8$) at stresses considerably below the fatigue limit determined by conventional test procedures ($N < 10^7$). A fracture mechanics approach to this problem was proposed by *Kitagawa* and *Takahashi* [13.112]. Based on a diagram relating a cyclic stress amplitude with crack length, a critical defect size ($a_t$) can be deduced which, when exceeded, causes a reduction of the fatigue strength. A modification of this diagram by introducing the value of the effective stress intensity range is shown in Fig. 13.43 [13.108]. Good agreement between predicted values and experimental results are obtained for hemispherical surface notches of various sizes [13.113, 114].

### 13.4.5 Creep Properties

Creep-rupture data available up to 1970 were collected in [13.1]. A review of creep information from 1960 to 2000 for Nb, Ta and Mo in the temperature range between 0.4 and $0.5T_M$ (in K) was presented in [13.115]

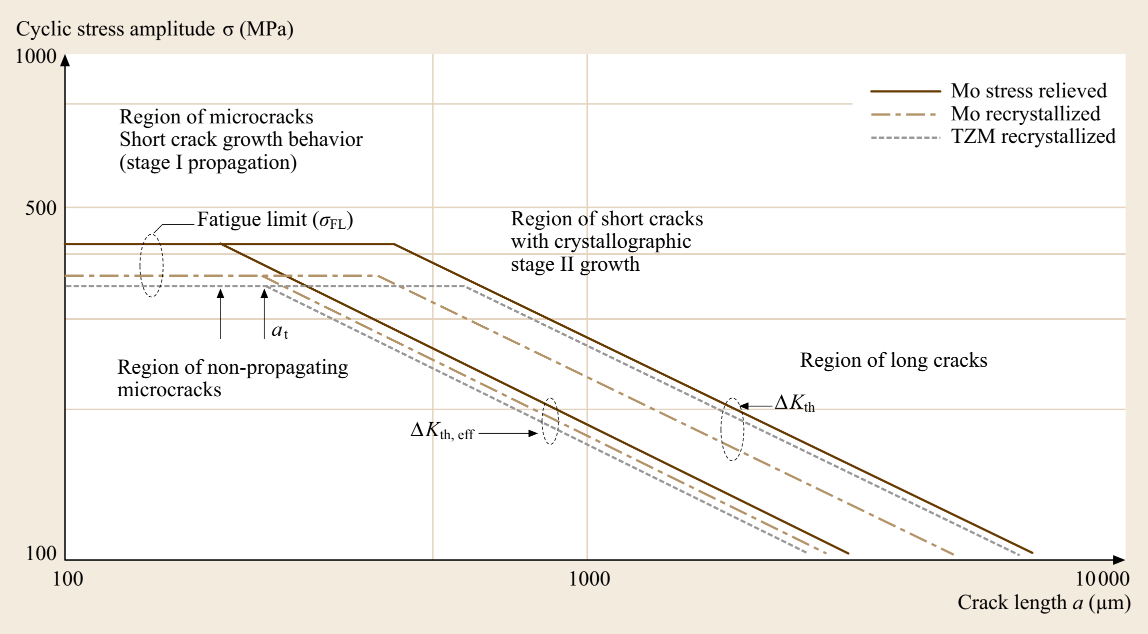


**Fig. 13.43** Effect of crack length on stress amplitude for crack growth in specimens of stress relieved Mo, recrystallized Mo, and recrystallized TZM (modified Kitagawa diagram) (after [13.108])

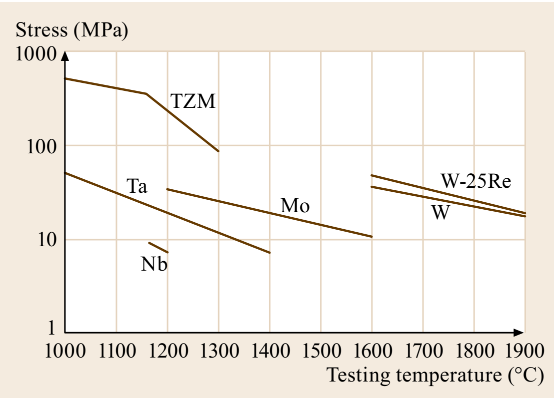


**Fig. 13.45** Comparison of 100 h of rupture data for selected refractory metals (after [13.1])

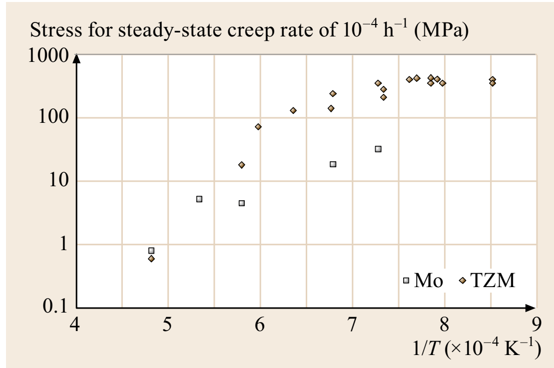


**Fig. 13.46** Stress for steady state creep rate of $1\times10^{-4}\,h^{-1}$ versus $1/T$ for Mo and TZM, deformed samples, various shapes (after [13.51])

revealing the creep behavior depending on composition, microstructure and test environment. Creep rupture data of Mo and W sheet material up to temperatures of 2500 °C were reported [13.116] showing the creep rate as function of testing temperature and applied stress.

The fairly wide scatter results from minor differences in microstructure, thermomechanical pretreatment, and impurity levels, but possibly also from impurities picked up from the environment in the high temperature test systems. A summary of 10 000 h/1% creep data for Mo, W, and TZM is given in Fig. 13.44; the 100 h creep-rupture data for Mo, W, Nb, Ta, W25Re and TZM are given in Fig. 13.45, based on [13.1]. Up to 1100 °C the carbide-precipitation-hardened material TZM reveals the highest creep strength, only outperformed by Mo and W alloys precipitation hardened with hafnium carbide, which are not considered in these figures. Comparing the stress causing a steady state creep rate of $1\times10^{-4}\,h^{-1}$, as illustrated in Fig. 13.46, it can be concluded that precipitation hardening is effective up to ≈ 1400 °C. At higher temperatures, the creep strength of TZM deteriorates to the level of Mo or even below. Above 1600 °C, W-based materials offer the best performance.

The influence of the microstructure on the creep mechanisms of Mo is illustrated in Fig. 13.47 for 1450 °C [13.117]. For a test stress of 35 MPa the steady state creep rate is almost independent of the grain size. In this stress regime a stress exponent of 5.4 was obtained, indicating dislocation creep as the rate-controlling mechanism. Lowering the test stress to 14 and 7 MPa, grain-size-dependent creep mechanisms, such as diffusion creep and grain boundary sliding, become active, and as a consequence, the steady state creep rate increases with decreasing grain size [13.117].

The steady state creep rates of Mo rods made of VAC ingots, VAC and P/M Mo sheets, and P/M Mo-0.7 wt% $La_2O_3$ sheets are summarized in Fig. 13.48.

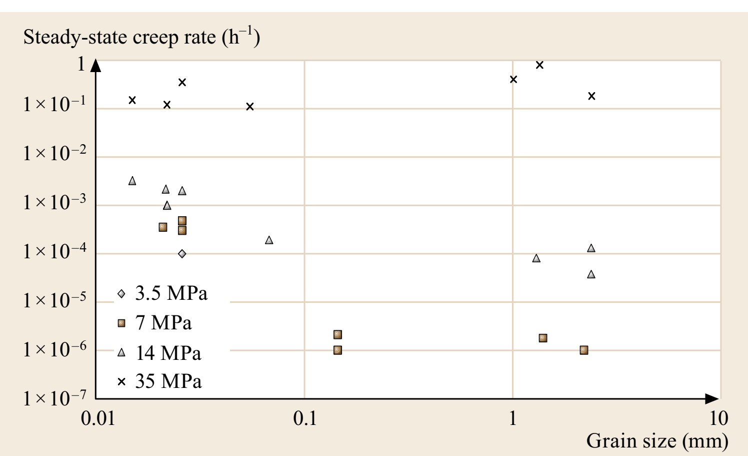


**Fig. 13.47** Steady-state creep rate of Mo sheets versus grain size. Sheet thickness = 2 mm/6 mm; testing temperature = 1450 °C; test atmosphere = hydrogen (after [13.117])

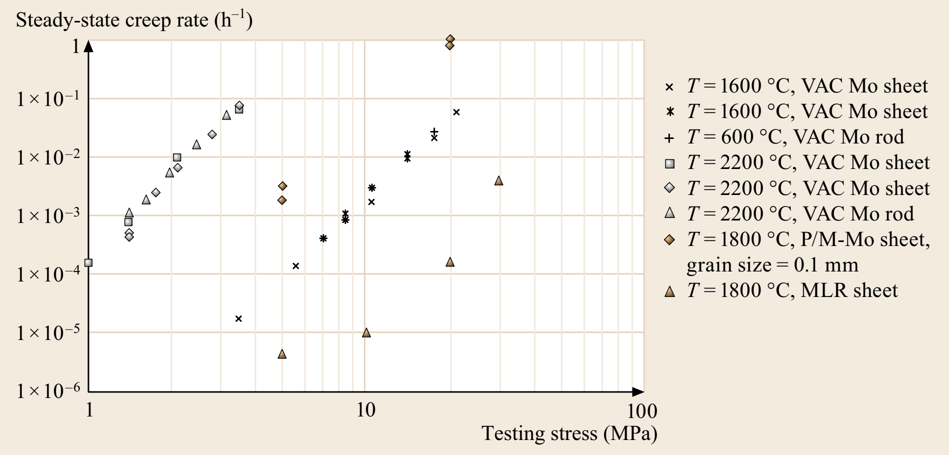


**Fig. 13.48** Steady-state creep rate at various testing temperatures of vacuum-arc-cast (VAC) Mo sheet (thickness = 0.5 mm), VAC Mo rod (diameter = 4.1 mm), P/M Mo sheet (thickness = 6 mm), and P/M Mo-0.7 wt% $La_2O_3$ (MLR) sheet (thickness = 1 mm) versus testing stress (after [13.1, 117])

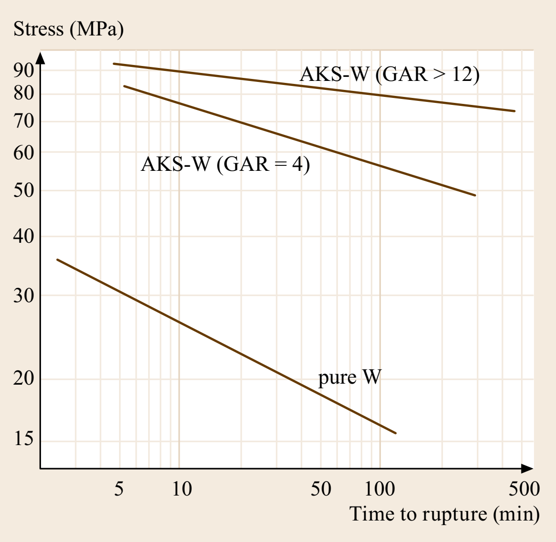


**Fig. 13.49** Creep rupture data for AKS-W wires in comparison with pure W. Wire diameter = 0.183 mm; testing temperature = 2527 °C; atmosphere = vacuum better than $7\times10^{-5}$ Pa; heating rate ≈ 2000 °C $s^{-1}$ (after [13.65])

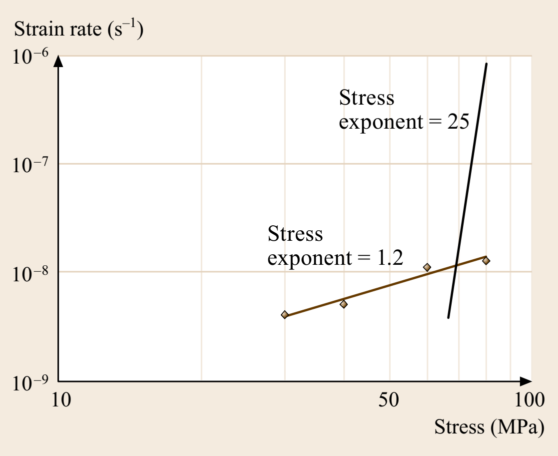


**Fig. 13.50** Strain rate versus stress for AKS-W wires tested at 2527 °C. *Wright* 1978 (after [13.65], *black line*): AKS-W wire with a diameter of 0.183 mm; atmosphere = vacuum better than $7\times10^{-5}$ Pa; heating rate ≈ 2000 °C $s^{-1}$; GAR = 35 ± 10; pre-recrystallized at 2527 °C/10 min. *Zilberstein* 1998 (after [13.118], *colored symbol*): AKS-W wire with a diameter of 0.178 mm; atmosphere = vacuum; GAR = 31 ± 1; pre-recrystallized at 2527 °C/15 min

Stress exponents of 4.3 (P/M Mo sheet/1800 °C), 4.5–4.7 (VAC Mo sheet/1600 °C), 4.6 (VAC Mo rod/1600 °C), 5.0 (Mo-0.7 wt% $La_2O_3$/1800 °C), and 5.5 (VAC Mo sheet/2200 °C) indicate that dislocation controlled creep is rate-controlling in the stress regime investigated.

For AKS-W wires, used as lamp filaments, creep resistance is one of the most important requirements. The fine bubbles stabilized at operating temperature with K-gas act as an effective barrier against dislocation movement, thereby reducing the deformation rate in the power-law creep regime. Nabarro–Herring and/or Coble creep is suppressed because of the large diffusion distances in a structure with large, highly elongated grains. Grain boundaries resist sliding because of the interlocking structure. A comparison of creep rupture data of pure W and two AKS-W grades with different grain aspect ratios (GAR) is given in Fig. 13.49.

In the high stress regime (> 60 MPa) and at temperatures between 2500 and 3000 °C, stress exponents between 8 and 25 were found [13.65, 119, 120]. This high stress dependence led to the introduction of a threshold stress ($\sigma_{th}$) below which a component does not reveal any measurable creep deformation under usual service conditions. For this threshold stress, which is lower than the Orowan stress, the detachment of the dislocations from the second phase particles or bubbles is the controlling factor [13.121, 122].

In the second phase particle–metal matrix interface, the dislocation line energy is lower compared to the dislocation line energy in the metal matrix. Of all dispersion strengthened materials investigated, K bubbles in AKS-W exert the most attractive interaction on dislocations [13.123].

For material produced in the 1970s with a mean, but strongly scattered, grain aspect ratio of around 35, dislocation creep dominated at stresses $> 60\,\mathrm{MPa}$ (stress exponent $= 25$), as can be seen in Fig. 13.50. For material produced 20 years later with a similar grain aspect ratio of 31, a stress exponent of 1.2 was found in the stress regime from 30 to 80 MPa, indicating a diffusion-controlled creep process [13.124]. The evaluation of the strain rate/stress dependence of the values generated under vacuum also reveals a stress exponent close to 1 [13.118]. Data for the stress exponents are summarized in [13.123].

By lowering the grain aspect ratio, the transition temperature between dislocation and diffusion creep is shifted towards lower stresses. In the low GAR regime a strong dependence of the creep resistance on microstructural features can be observed, as grain boundary related phenomena, such as grain boundary sliding and diffusion creep resulting in cavitations become rate-controlling. The influence of the GAR value on time to creep rupture is demonstrated in Fig. 13.51.

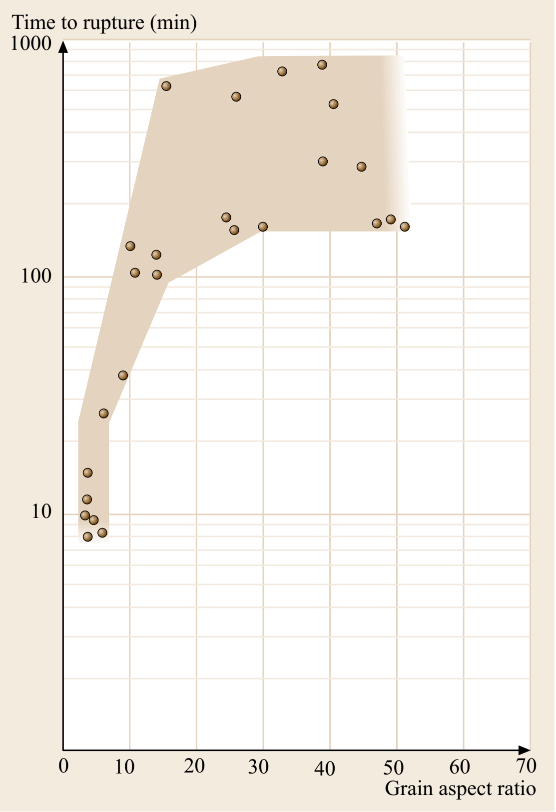


**Fig. 13.51** Time-to-rupture versus grain aspect ratio for AKS-W wires with a diameter of 0.183 mm. Testing temperature $= 2527\,^{\circ}\mathrm{C}$; test stress $= 73.6\,\mathrm{MPa}$; atmosphere = vacuum better than $7\times10^{-5}\,\mathrm{Pa}$; heating rate $\approx 2000\,^{\circ}\mathrm{C\,s^{-1}}$ (after [13.65])

## References


13.1 J.B. Conway, B.N. Flagella: *Creep Rupture Data for the Refractory Metals to High Temperatures* (Gordon Breach, New York 1971)

13.2 R. Kieffer, G. Jangg, P. Ettmayer: *Sondermetalle* (Springer, Vienna 1971)

13.3 American Society for Metals: *Properties and Selection: Nonferrous Alloys and Pure Metals*, Metals Handbook New Series, Vol. 2, 9th edn. (American Society for Metals, Metals Park 1979)

13.4 W.C. Hagel, J.A. Shields, S.M. Tuominen: Processing and production of molybdenum and tungsten alloys. In: *Proc. Symp. Refract. Technol. Space Nucl. Power Appl., CONF-8308130, Oak Ridge National Laboratory* (1983) p. 98

13.5 K.H. Miska, M. Semchyshen, E.P. Whelan (Eds.): *Physical Metallurgy and Technology of Molybdenum and its Alloys* (AMAX, Michigan 1985)

13.6 J. Wadsworth, T.G. Nieh, J.J. Stephens: Recent advances in aerospace refractory metal alloys, Int. Mater. Rev. **33**(3), 131 (1988)

13.7 E. Pink, I. Gaal: Mechanical properties and deformation mechanisms of non-sag tungsten wires. In: *The Metallury of Doped, Non-Sag Tungsten*, ed. by E. Pink, L. Bartha (Elsevier, New York 1989) p. 209

13.8 T.G. Nieh, J. Wadsworth: Recent advances and developments in refractory alloys, Mater. Res. Soc. Symp. Proc. **322**, 315 (1994)

13.9 E. Pink, R. Eck: Refractory metals and their alloys. In: *Materials Science and Technology – A Comprehensive Treatment*, Vol. 8, ed. by R.W. Cahn, P. Haasen, E.J. Kramer (VCH, Weinheim 1997) p. 589

13.10 E. Lassner, W.D. Schubert: *Tungsten: Properties, Chemistry, Technology of the Element, Alloys, and Chemical Compounds* (Kluwer/Plenum, New York 1999)

13.11 G. Leichtfried: *Handbook of Extractive Metallurgy* (Wiley-VCH, Weinheim 1997) p. 1371

13.12 G. Leichtfried: *Powder Metallurgy Data*, Landolt–Börnstein, New Series, Vol. VIII/2A (Springer, Berlin, Heidelberg, New York 2002)

13.13 G. Leichtfried: Molybdenum lanthanum oxide: Special material properties by dispersoid refining during deformation. In: *Advances in Powder Metallurgy and Particulate Materials*, Vol. 9 (MPIF, Princeton 1992) p. 123

13.14 M.K. Yoo, Y. Hiraoka, J. Chu: Recrystallization of Mo wire doped with lanthanum oxide, Int. J. Refract. Metal. Hard Mater. **13**(4), 221 (1995)

13.15 A.J. Mueller, R.W. Buckman, A.J. Shields Jr.: The effect of TM-processing on the mechanical properties of Mo-2% lanthana. In: *Proc. 15th Int. Plansee Semin.* (Plansee AG, Reutte 2001)

13.16 G.-J. Zhang, Y.-J. Sun, F. Jiang, L. Wang, R. Wang, J. Sun: Microstructure and strenghening mechanisms of Mo-alloy wires doped with lathanum oxide particles, Int. J. Refract. Met. Hard Mat. **27**(1), 173 (2009)

13.17 D.M. Moon, R.C. Koo: Mechanism and kinetics of bubble formation in doped W, Metall. Mater. Trans. B **2**, 2125 (1971)

13.18 H.G. Sell, D.F. Stein, R. Stickler, A. Joshi, E. Berkey: The identification of bubble forming impurities in doped tungsten, J. Inst. Met. **100**, 275 (1972)

13.19 P. Makarov, K. Povarova: Principles of the alloying of tungsten and development of the manufacturing technology for the tungsten alloys. In: *Proc. 15th Plansee Semin.*, Vol. 3 (Plansee AG, Reutte 2001) p. 464

13.20 G.A. Geach, J.E. Hughes: The alloy of rhenium with molybdenum or with tungsten and having good high temperature properties. In: *Proc. 2nd Plansee Semin.* (Plansee AG, Reutte 1955) p. 245

13.21 R.I. Jaffee, C.T. Sims, J.J. Harwood: The effect of rhenium on the fabricability and ductility of molybdenum and tungsten. In: *Proc. 3rd Plansee Semin.* (Plansee AG, Reutte 1958) p. 380

13.22 J.G. Booth, R.I. Jaffee, E.I. Salkovitz: The mechanisms of the rhenium-alloying effect in group VI-A metals. In: *Proc. 5th Plansee Semin.* (Plansee AG, Reutte 1964) p. 547

13.23 Plansee Aktiengesellschaft: Internal Material Data Base (Reutte 2000)

13.24 H. Borchers, E. Schmidt (Eds.): *Stoffwerte und Verhalten von metallischen Werkstoffen*, Landolt–Börnstein, New Series, Vol. IV/2b, 6th edn. (Springer, Berlin, Heidelberg 1964)

13.25 T.E. Tietz, J.W. Wilson: *Behavior and Properties of Refractory Metals* (Stanford Univ. Press, Stanford 1965) p. 325

13.26 Plansee Aktiengesellschaft: Tungsten Company Brochure (Reutte 1997)

13.27 C. Cagran, C. Brunner, A. Seifter, G. Pottlacher: Liquid-phase behaviour of normal spectral emissivity at 684.5 nm of some selected metals, High Temp. High Press. **34**, 669 (2002)

13.28 Dechema-Werkstoff-Tabelle: *Oxidierende Heißgase* (Dechema, Frankfurt 1981)

13.29 S.P. Murarka: *Silicides for VLSI Applications* (Academic, New York 1983), p. 73, 151

13.30 Y. Kuo (Ed.): *Thin Film Transistors – Materials and Processes*, Amorphous Silicon Thin Film Transistors New Series, Vol. 1 (Kluwer, Dordrecht 2004) p. 335

13.31 W.N. Shafarman, J.E. Phillips: Direct current-voltage measurements of the Mo/$CuInSe_2$ contact on operating solar cells. In: *Proc. 25th IEEE Photovolt. Conf.* (1996) p. 917

13.32 A. Schintlmeister, H.-P. Martinz, P. Wilhartitz, F.P. Netzer: Low-temperature oxidation of industrial molybdenum surfaces. In: *Powder Metall. World Congr. Exhib.* (EPMA, Granada 1998) p. 526

13.33 G. Leichtfried: *Powder Metallurgical Components for Light Sources*, Habilitation Thesis (Montanuniversität, Leoben 2003)

13.34 A. List, C. Mitterer, G. Mori, J. Winkler, N. Reinfried, W. Knabl: Oxidation of sputtered thin films of molybdenum alloys at ambient conditions. In: *Proc. 17th Plansee Semin.*, Vol. 1 (Plansee Group, Reutte 2009), RM12/1

13.35 E. Fromm, E. Gebhardt: *Gase und Kohlenstoff in Metallen* (Springer, Berlin, Heidelberg 1976) p. 747, in German

13.36 R. Speiser, G.R. St. Pierre: Proc. AGARD (Advisory Group for Aerospace Research and Development) Conf. on refractory metals, Oslo (1963)

13.37 J. Disam, H.-P. Martinz, M. Sulik: Layer for protection against oxydation, European Patent Specification EP 0 798 402 B1 (1997)

13.38 C.A. Krier: *Coatings for the Protection of Refractory Metals from Oxidation*, Defense Metals Information Center Report New Series, Vol. 162 (Battelle Memorial Institute, Columbus 1961)

13.39 W. Knabl: *Oxidationsschutz von Refraktärmetallen auf der Basis von Silizid- und Aluminidschichten*, Ph.D. Thesis (Montanuniversität, Leoben 1995), in German

13.40 H.-P. Martinz, M. Sulik: Oxidation protection of refractory metals in the glass industry, Glastech. Ber., Glas Sci. Technol. **73**(C2), 299 (2000)

13.41 C. Stickler: *Mikroplastizität und zyklisches Spannungs- Dehnungsverhalten von Ta und Mo bei Temperaturen unter* $0.2T_m$, Ph.D. Thesis (Univ. Vienna, Vienna 1998)

13.42 S. Primig, H. Leitner, H. Clemens, A. Lorich, W. Knabl, R. Stickler: On the recrystallization behavior of technically pure Mo, Int. J. Refract. Metall. Hard Mater. **28**, 703 (2010)

13.43 S. Primig, H. Leitner, H. Clemens, A. Lorich, W. Knabl, R. Stickler: SEM and TEM Investigations of recovery and recrystallization in technically pure Mo, Prakt. Metallogr. **48**, 7 (2011)

13.44 S. Primig, H. Leitner, H. Clemens, A. Lorich, W. Knabl, R. Stickler: Influence of the heating rate on the recrystallization behvior of Mo, Mater. Sci. Eng. A **535**, 316 (2012)

13.45 E. Pink: Rekristallisationsdiagramme von gesintertem Mo und W, Planseeber. Pulvermetall. **13**, 100 (1965)

13.46 E. Pink, H. Kärle: Zum Rekristallisationsverhalten von Sintertantal, Planseeber. Pulvermetall. **16**, 105

(1968)
13.47 G. Leichtfried, G. Thurner, R. Weirather: Molybdenum alloys for glass-to-metal seals. In: *Proc. 14th Plansee Semin.*, Vol. 4 (Plansee AG, Reutte 1997) p. 26
13.48 H.H.R. Jansen: The recrystallization texture of nonsag wire. In: *The Metallurgy of Doped, Non-Sag Tungsten*, ed. by E. Pink, L. Bartha (Elsevier, New York 1989) p. 203
13.49 D.B. Snow: The recrystallization of non-sag tungsten wire. In: *The Metallurgy of Doped, Non-Sag Tungsten* (Elsevier, New York 1989) p. 189
13.50 V.I. Trefilov, Y.V. Milman: Physical basis of thermomechanical treatment of refractory metals. In: *Proc. 12th Plansee Semin.*, Vol. 1 (Plansee AG, Reutte 1989) p. 107
13.51 E. Parteder, W. Knabl, R. Stickler, G. Leichtfried: Bruchzähigkeit und Porenverteilung von Molybdän Stabmaterial in Abhängigkeit des Reckgrades und des Rekristallisationsgrades. In: *Proc. 14th Plansee Semin.*, Vol. 1 (Plansee AG, Reutte 1997) p. 984
13.52 E. Parteder, H. Riedel, R. Kopp: Densification of sintered molybdenum during hot upsetting: Experiments and modeling, Mater. Sci. Eng. A **264**, 17 (1999)
13.53 E. Parteder: *Ein Modell zur Simulation von Umformprozessen pulvermetallurgisch hergestellter hochschmelzender Metalle*, Ph.D. Thesis (RWTH, Aachen 2000)
13.54 E. Parteder, H. Riedel: Simulating of hot forming processes of refractory metals using porous metal plasticicty models. In: *Proc. 15th Plansee Semin.*, Vol. 3 (Plansee AG, Reutte 2001) p. 60
13.55 B.P. Bewlay, C.L. Briant: Discussion of "evidence for the existence of potassium bubbles in AKS-doped tungsten wire" and reply, Metall. Mater. Trans. A **22**, 2153 (1991)
13.56 C.L. Briant: The effect of thermomechanical processing on the microstructure of tungsten rod. In: *Proc. 13th Plansee Semin.*, Vol. 1 (Plansee AG, Reutte 1993) p. 321
13.57 J.L. Walter, C.L. Briant: Tungsten wire for incandescent lamps, J. Mater. Res. **5**, 2004 (1990)
13.58 G.L. Krasko: Effect of impurities on the electronic structure of grain boundaries and intergranular cohesion in tungsten. In: *Proc. 13th Plansee Semin.*, Vol. 1 (Plansee AG, Reutte 1993) p. 27
13.59 A. Kumar, B.L. Eyre: Grain boundary segregation and intergranular fracture in molybdenum, Proc. R. Soc. A **370**, 431 (1980)
13.60 P. Wilhartitz, G. Leichtfried, H.P. Martinz, H. Hutter, A. Virag, M. Grasserbauer: Applications of 3D-SIMS for the development of refractory metal products. In: *Proc. 2nd Euro. Conf. Adv. Mater. Process.*, ed. by T.W. Clyne, P.J. Withers (1992) p. 323
13.61 J. Femböck, R. Stickler, A. Vinckier: The effect of strain rate and heating rate on the tensile behavior of W and W-$ThO_2$ between room temperature and 1400°C. In: *Proc. 11th Plansee Semin.*, Vol. 1 (Plansee AG, Reutte 1985) p. 361
13.62 D.L. Chen, B. Weiss, R. Stickler, M. Witwer, G. Leichtfried, H. Hödl: Fracture toughness of high melting point materials. In: *Proc. 13th Plansee Semin.*, Vol. 1 (Plansee AG, Reutte 1993) p. 621
13.63 E.S. Meiren, D.A. Thomas: Effect of grain boundaries on the bending ductility of tungsten, Metall. Trans. **233**, 937 (1965)
13.64 P.F. Browning, C.L. Briant, B.A. Knudsen: Dependence of material properties on processing history during wire drawing of commercially doped tungsten lamp wire. In: *Proc. 13th Plansee Semin.*, Vol. 1 (Plansee AG, Reutte 1993) p. 336
13.65 P.K. Wright: High temperature creep behavior of doped tungstenwire, Metall. Trans. **9**, 955 (1978)
13.66 J. Neges, B. Ortner, G. Leichtfried, H.P. Stüwe: On the 45° embrittlement of tungsten sheets, Mater. Sci. Eng. A **196**, 129 (1995)
13.67 Y.V. Milman: unpublished results
13.68 St M. Cardonne: Tantalum and its alloys, Adv. Mater. Process. **9**, 16 (1992)
13.69 H. Ullmaier: Design properties of tantalum or everything you always wanted to know about tantalum but were afraid to ask, ESS (European Spallation Source) Report ISSN 1433-559X, 03-131-T (2003)
13.70 A. Seeger: The temperature dependence of the critical shear stress and of work hardening of metal crystals, Philos. Mag. **7**, 771 (1954)
13.71 J.W. Christian: Plastic deformation of bcc metals. In: *Proc. Int. Conf. Strength Mater. (ICSMA-2), Asilomar* (ASTM, Philadelphia 1970) p. 31
13.72 H. Mughrabi: unpublished results
13.73 W. Rinnerthaler, F. Benesovsky: Untersuchungen über das Mikrodehnungsverhalten von Molybdän, Planseeber. Pulvermetall. **21**, 253 (1973)
13.74 C. Stickler, D.L. Chen, B. Weiss, R. Stickler: Time dependent microplastic deformation of Mo and Ta at low temperatures. In: *Proc. 14th Plansee Semin.*, Vol. 1 (Plansee AG, Reutte 1997) p. 1004
13.75 K.J. Bowman, R. Gibala: Cyclic deformation of W single crystals, Scr. Metall. **20**, 1451 (1986)
13.76 M.A. Meyers, Y.-J. Chen, F.D.S. Marquis, D.S. Kim: High-strain, high-strain-rate behavior of tantalum, Metall. Mater. Trans. A **26**, 2493 (1995)
13.77 C.C. Wojcik: Thermomechanical processing and properties of niobium alloys. In: *Proc. Int. Symp. Niobium, Orlando* (2001) p. 163
13.78 H. Mughrabi, K. Herz, X. Stark: Cyclic deformation and fatigue behavior of $\alpha$-Fe mono- and polycrystals, Int. J. Fract. **17**, 193 (1981)
13.79 M. Werner: Temperature and strain rate dependence of the flow stress of Ta single crystals in cyclic deformation, Rev. Phys. Appl. **23**, 672 (1988)
13.80 J. Femböck, K. Pfaffinger, B. Weiss, R. Stickler: Verhalten von Mo-Werkstoffen unter zyklischer Beanspruchung. In: *Proc. 10th Plansee Semin.*, Vol. 2 (Plansee AG, Reutte 1981) p. 27
13.81 K. Pfaffinger, J. Femböck: Versuchsplanung und statistische Auswertung von Schwingfestigkeitsdaten von Mo-Werkstoffen. In: *Proc. 10th Plansee Semin.*, Vol. 2 (Plansee AG, Reutte 1981) p. 233

13.82 K. Mecke, C. Holste, W.F. Terentjev: Dislocation arrangement in cyclically deformed polycrystalline molybdenum, Cryst. Res. Technol. **15**, 83 (1980)
13.83 S. Kong, B. Weiss, R. Stickler, M. Witwer, H. Hödl: Cyclic stress strain behavior of high melting point metals. In: *Proc. 13th Plansee Semin.*, Vol. 1 (Plansee AG, Reutte 1993) p. 720
13.84 D.R. Helebrand, R.I. Stephens: Cyclic yield behavior of Ta, J. Mater. Sci. **7**, 530 (1972)
13.85 C. Stickler, W. Knabl, R. Stickler, B. Weiss: Cyclic behavior of Ta at low temperatures under low stresses and strain rates. In: *Proc. 15th Plansee Semin.*, Vol. 3 (Plansee AG, Reutte 2001) p. 34
13.86 J.M. Meiniger, J.C. Gibeling: LCF of Nb and Nb-1Zr alloys, Metall. Trans. A **23**, 3077 (1992)
13.87 M. Papakyriacou, H. Mayer, C. Pypen, H. Plenk, S. Stanzl-Tschegg: Influence of loading frequency on high cycle fatigue properties of bcc and hcp metals, Mater. Sci. Eng. A **308**, 143 (2001)
13.88 H.A. Calderon, G. Kostorz: Microstructure and plasticity of two molybdenum-base alloys (TZM), Mater. Sci. Eng. A **A160**, 189 (1993)
13.89 H.J. Shi, L.S. Niu, C. Korn, G. Pluvinage: High temperature fatigue behavior of Mo-TZM alloy under mechanical and thermomechanical cyclic load, J. Nucl. Mater. **278**, 328 (2000)
13.90 R.F. Brodrick: LCF-data of P/M-W between 1650 and 3300°C, Proc. ASTM **64**, 505 (1965)
13.91 S.S. Manson: *Thermal Stress and Low Cycle Fatigue* (McGraw-Hill, New York 1981) p. 187
13.92 R.E. Schmunk, G.E. Korth, M. Ulrickson: Tensile and LCF measurements on cross rolled tungsten, J. Nucl. Mater. **103**, 943 (1981)
13.93 T. Kimishima, M. Sukekawa, K. Owada, M. Shimizu: Fatigue data of Mo. In: *9th Symp. Eng. Probl. Fusion Res.* (IEEE, New York 1981) p. 255
13.94 H. Nishi, T. Oku, T. Kodeira: Influence of microstructural change caused by cyclic strain on the LCF strength of sintered Mo, Fusion Eng. Des. **9**, 123 (1989)
13.95 Z.M. Sun, Z.G. Wang, H. Hödl, R. Stickler, B. Weiss: Low cycle fatigue and creep behavior of recrystallized Mo near room temperature, Materialwiss. Werkstofftech. **26**, 483 (1995)
13.96 J.A. Shields, P. Lipetzly, A.J. Mueller: Fracture toughness of 6.4 mm arc cast Mo and TZM Plate at RT and 300°C. In: *Proc. 15th Plansee Semin.*, Vol. 4 (Plansee AG, Reutte 2001) p. 187
13.97 B.V. Cockeram: Measuring the fracture toughness of Mo-0.5%Ti-0.1%Zr using standard and subsized bend specimens, Metall. Mater. Trans. A **33**(12), 3685 (2002)
13.98 M. Faleschini, H. Kreuzer, D. Kiener, R. Pippan: Fracture toughness investigations of W-alloys, J. Nucl. Mater. A **367–370**, 800 (2007)
13.99 B. Gludovatz, S. Wurster, A. Hoffmann, R. Pippan: Fracture toughness of polycrystalline W alloys, Int. J. Refract. Metal. Hard Mater. **28**(6), 674 (2010)
13.100 C.W. Marschall, F.C. Holden: Fracture toughness of refractory metals and alloys. In: *High Temperature Refractory Metals*, ed. by L. Richardson (Gordon Breach, New York 1964) p. 129
13.101 M. Rödig, H. Derz, G. Pott, B. Werner: Fracture mechanics investigations of TZM and Mo5Re. In: *Proc. 14th Plansee Semin.*, Vol. 1 (Plansee AG, Reutte 1997) p. 781
13.102 D. Padhi, J.J. Lewandowski: Effects of test temperature and grain size on the charpy impact toughness and dynamic toughness (KID) of polycrystalline niobium, Metall. Mater. Trans. A **34**, 967 (2003)
13.103 J.X. Zhang, L. Liu, M.L. Zhou, Y.C. Hu, T.Y. Zuo: Fracture toughness of sintered Mo-$La_2O_3$, Inter. J. Refract. Metall. Hard Mater. **17**, 405 (1999)
13.104 D.L. Chen, B. Weiss, R. Stickler: The effective fatigue threshold: Significance of the loading cycle below the crack opening load, Int. J. Fatigue **16**, 485 (1994)
13.105 J. Riedle: Bruchwiderstand in Wolfram-Einkristallen: Einfluß der kristallographischen Orientierung, der Temperatur und der Lastrate. In: *Fortschrittsberichte VDI, Reihe 18, Mechanik/Bruchmechanik*, Vol. 184 (VDI, Düsseldorf 1995)
13.106 R. Pippan: *Bruchzähigkeitsuntersuchungen an W Proben* (Erich Schmid Institut, Leoben 1999)
13.107 Y. Mutoh, K. Ichikawa, K. Nagata, M. Takeuchi: Effect of Re addition on fracture toughness of W at elevated temperatures, J. Mater. Sci. **30**, 770 (1995)
13.108 A. Fathulla, B. Weiss, R. Stickler: Short fatigue cracks in technical P/M-Mo alloys. In: *The Behavior of Short Fatigue Cracks, Mechanical Engineering Publications*, Vol. 1 (EGF, Suffolk 1986) p. 115
13.109 R. Grill, H. Clemens, P. Rödhammer, A. Voiticek: P/M processing, characterization and application of Ta-10W. In: *Proc. 14th Plansee Semin.*, Vol. 4 (Plansee AG, Reutte 1997) p. 211
13.110 R. Heidenreich, R. Schäfer, H. Clemens, M. Witwer: Mechanical properties of high-temperature fasteners from refractory alloys. In: *Proc. 13th Plansee Semin.*, Vol. 1 (Plansee AG, Reutte 1993) p. 664
13.111 A. Fathulla, B. Weiss, R. Stickler, J. Femböck: The initiation and growth of short cracks in PM-Mo. In: *Proc. 11th Plansee Semin.*, Vol. 1 (Plansee AG, Reutte 1985) p. 45
13.112 H. Kitagawa, S. Takahashi: Applicability of fracture mechanics to very small cracks or the cracks in the early stage. In: *Proc. Second Int. Conf. Mech. Behav. Mater.* (ASM, Metals Park 1976) p. 627
13.113 B. Weiss, R. Stickler: Methods for predicting the fatigue strength of P/M-materials. In: *Proc. Int. Powder Metall. Conf. PM'88, Orlando* (1988) p. 3
13.114 B. Weiss, R. Stickler, A.F. Blom: A model for the description of the influence of small 3-dimensional defects on the HCF limit. In: *Proc. Conf. Short Fatigue Cracks, Sheffield, 1990* (Mechanical Engineering, Suffolk 1992) p. 423
13.115 R.W. Buckman: The creep behavior of refractory metal alloys, Int. J. Refract. Metal. Hard Mater. **18**(4/5), 253 (2000)
13.116 B. Fischer, S. Vorberg, R. Voekl, M. Beschliesser, A. Hoffmann: Creep and tensile tests on refracrory metals at extremely high temperatures, Int. J. Re-

fract. Metal Hard Mater. **24**(4), 292 (2006)
13.117 G. Leichtfried: *Die Entwicklung von kriechfesten Molybdän-Seltenerdoxid-Werkstoffen für Hochtemperaturanwendungen*, Ph.D. Thesis (Montanuniversität, Leoben 1997)
13.118 G. Zilberstein: Creep properties of non-sag tungsten recrystallized in stagnant oxygen-doped argon, Int. J. Refract. Metall. Hard Mater. **16**, 71 (1998)
13.119 D.M. Moon, R. Stickler: Creep behavior of fine wires of P/M pure, doped and thoriated tungsten, High Temp. High Press. **3**, 503 (1971)
13.120 J.W. Pugh: On the short time creep rupture properties of lamp wire, Metall. Trans. **4**, 533 (1973)
13.121 J.H. Schröder, E. Arzt: Weak beam studies of dislocation/dispersoid interaction in an ODS superalloy, Scr. Metall. **19**, 1129 (1985)
13.122 J. Rössler, E. Arzt: Kinetics of dislocation climb over hard particles – Climb without attractive particle-dislocation interaction, Acta Metall. **36**, 1043 (1988)
13.123 J. Rössler, E. Arzt: A new model-based creep equation for dispersion strengthened materials, Acta Metall. Mater. **38**(4), 671 (1990)
13.124 G. Zilberstein, J. Selverian: Creep deformation of non-sag tungsten in argon doped with low oxygen concentrations. In: *Proc. 13th Plansee Semin.*, Vol. 1 (Plansee AG, Reutte 1993) p. 132